Assessing the geographic distribution and conservation status of *Heuchera alba* and *Heuchera pubescens* using field surveys, morphology and genomics methods

Anais Barnes[1], Madeline Wickers[1], Tanisha M. Williams[1], Scott Schuette[2], Chris Martine[1]
1 Bucknell University Department of Biology Lewisburg, PA; 2 Western Pennsylvania Conservancy, Pittsburgh, PA

Key Questions

- Which species do the populations found in Pennsylvania belong to, *H. pubescens* or *H. alba*?
- Are the populations expected to be *H. alba* genetically healthy?
- What is the identification of the primary pollinator associated with *H. alba*?

Introduction

Heuchera, a genus of 43 species in the Saxifragaceae family endemic to North America, contains a variety of species which are often difficult to distinguish morphologically. Similarities among species are sometimes due to sympatric hybridization between species, which has caused confusion in defining boundaries relating to taxonomy [1]. This uncertainty has led to challenges in determining geographic distributions of similar taxa and definitive identification of the species within the Northeast region. Within Pennsylvania, two species are historically recognized throughout the state: *Heuchera americana* and *H. pubescens* [2]. However, a third species previously unknown for the state was found by Drs. Chris Martine and Scott Schuette in 2017 and later identified by Dr. Ryan Folk through social media, and this species was the globally-imperiled *H. alba* (white alumroot) [2,4] - the morphologically-similar sister species to *H. pubescens* previously only known from parts of Virginia and West Virginia.

As *H. americana* and *H. pubescens* were thought to be the only species within Pennsylvania, *H. alba* was not listed in The Plants of Pennsylvania [3] nor has there been an update in online databases for *H. alba* to include the expanded distribution of the species. The scope of our research is something that would possibly lead to this update and help identify the locations that were overlooked for *H. alba.* In this study, we assess the geographic distribution of *H. alba* along a portion of the Appalachian Ridge in Pennsylvania by a) visiting known localities (based on herbarium records) for *H. alba* and *H. pubescens* and b) tracking appropriate habitat to find previously unrecorded *H. alba* (or *H. pubescens*) localities. We then intend to assess whether these populations are genetically healthy in order to help create a conservation plan for them.

As part of our surveys, we also conducted pollinator observations with particular focus on the alumroot cellophane bee, *Colletes aestivali*s. Until recently, this species had not been seen in Pennsylvania since 1918.

Figure 1 Example of *Heuchera alba* (A) at a site in Northumberland County (B), growing at the top of the cliff at Shikellamy State Park, and (C) *H. alba* habitat

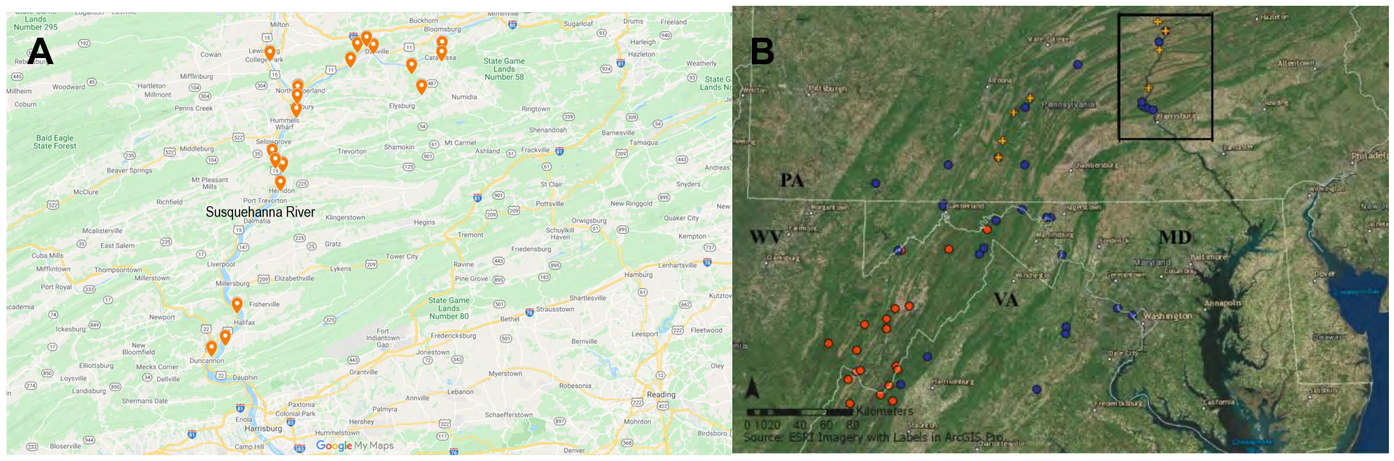

Figure 2. (A) Map of the 20 Pennsylvania collection sites visited this summer in the Susquehanna River Valley; (B) Map from Schuette, et al. (2018) showing previous understanding of distributions of *H. pubescens* (blue dots), pre-2017 *H. alba* (orange), and new 2017 *H. alba* localities. Black box shows Susquehanna Valley area covered in Map A. Note that all blue dots in the valley are now attributable to *H. alba*.

Bees

Colletes aestivalis, also known as the alumroot cellophane bee, is a ground-nesting specialist pollinator on *Heuchera*. Previous to 2019, this species had not been recorded in Pennsylvania since 1918. In June 2019, bees suspected to be *C. aestivalis* were collected from five *Heuchera alba* populations by Scott Schuette, Christopher Tracey, and Chris Martine. These specimens were eventually identified as *C. aestivalis* in the spring of 2021 by entomologist Mike Slater, confirming the first state records in 101 years and first occurrences of the bee on *Heuchera alba*. Over the summer of 2021, Anais and Maddie have collected seven bees from six different sites that appear to also be *C. aestivalis* (pending confirmation from Mike Slater), suggesting that just about any healthy population of *H. alba* in the Susquehanna Valley likely also supports a population of *C. aestivalis*. We suspect that our future population genetics results for *H. alba* may reflect the reliance of these plants on site-specific oligolectic bees for much of their pollination.

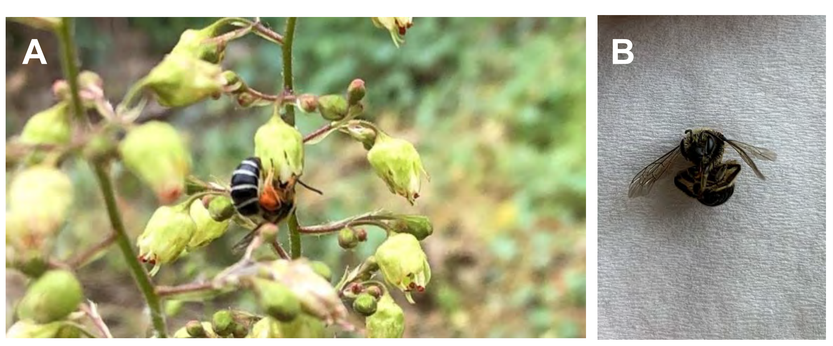

Figure 3. *Colletes* cf. *aestivalis* (alumroot cellophane bee) (A) foraging on *H. alba*, and (B) close-up.

Key Findings

- *Heuchera alba* is much more common in the state of Pennsylvania than previously thought. Through our research this summer it has been determined that all PA Susquehanna Valley records for *H. pubescens* appear to actually be attributable to *H. alba*. *H. alba* can best be described as a central Appalachian endemic that reaches the northern extent of its range in central Pennsylvania.
- *Heuchera alba* is associated with open, sheer rock faces/cliffs within the Valley/Ridge fold/thrust belt (deformed Paleozoic sedimentary strata) (as per Jeff Trop, pers. comm.). In the Susquehanna River Valley, the species is often encountered where this geology is exposed on riversides, roadsides, and railroad corridors.

Figure 4 Anais and Maddie at an *H. alba* field site in Pennsylvania.

Looking Forward

- Population genetics analysis
- Locating more populations based on ecological modeling informed by our new collections
- Working with the Western Pennsylvania Conservancy to update the conservation status of *H. alba*

References

1. Wells EF (1984) A revision of the genus *Heuchera* (Saxifragaceae) in eastern North America. Systematic Botany Monographs 3: 45–121. https://doi.org/10.2307/25027594.
2. Schuette S, Folk RA, Cantley JT, Martine CT (2018) The hidden *Heuchera*: How science Twitter uncovered a globally imperiled species in Pennsylvania, USA. PhytoKeys 96: 87-97. https://doi.org/10.3897/phytokeys.96.23667.
3. Rhoads AR, Block TA (2007) The Plants of Pennsylvania: An Illustrated Manual (2nd edition). University of Pennsylvania Press, Philadelphia, Pennsylvania, 498–499.
4. Martine CT (2017) (@MartineBotany) *Bombus* on *Heuchera americana*. Shikellamy Bluffs, PA 6 June 2017, 7:13 am. Tweet.

Support: David Burpee Endowment and the Wayne Manning Internship Fund

Bucknell UNIVERSITY BIOLOGY DEPARTMENT

Cross-linker density tunes the mechanics and structural organization of actin networks

Mike Dwyer and Bekele Gurmessa
Bucknell University Department of Physics and Astronomy, Lewisburg, PA 17837

Abstract: Actin, a globular protein, is a major component of cytoskeleton. In the presence of ATP and magnesium, G-actin polymerizes into filamentous actin (F-actin). F-actin plays crucial structural and mechanical roles in cell stability, motion, replication, and muscle contraction. Most of these mechanically driven structural changes in cells stem from the complex viscoelastic nature of entangled actin networks and the presence of a myriad of proteins that cross-link actin filaments. Despite its importance, the mechanical response of actin networks are not well understood, particularly at the molecular level. Here, we use optical trapping-coupled with fluorescence microscopy techniques to characterize the response of alpha-actinin cross-linked actin networks to localized microscale mechanical perturbations. In particular, we actively drive a microsphere 10 micrometers through cross-linked actin networks at a constant speed and measure the resistive force that the deformed actin filaments exert on the bead during and following strain. We determine the viscoelastic response of the cross-linked network by varying the concentration of cross-linking protein. Furthermore, we capture high-speed videos of the network via fluorescence laser scanning confocal microscopy to study the networks' structural change and heterogeneity as the density of cross-linking protein increases. Our results shed light on how cells undergo morphological changes through varying the cross-linker densities..

Procedure: Actin monomers (Cytoskeleton, AKL99) suspended in G-buffer [2 mM Tris, pH 8.0, 0.2 m ATP, 0.5 mM DTT, and 0.1 mM $CaCl_2$] are polymerized in F-buffer [10 mM Imidazole, pH 7.0, 50 mM KCl, 1 mM $MgCl_2$, 1 mM EGTA, 0.2 mM ATP]. Assembly of the network took place in a custom-built flow cell. A fixed concentration of 5.8 μM actin and a trace amount of 4.19 μm (diameter) fluorescently labeled polystyrene beads are mixed and actin is allowed to polymerize and cross-link for 30 min before measurement. Force data is collected by optically driving the microspheres through actin networks at constant speeds (5 and 10 μm/s) over 10 μm distance. Further, we collected three-dimensional image stacks (*z*-stacks, step size of 0.5 μm) of the fluorescently labeled networks using laser scanning confocal microscopy to resolve the network, filament structure and dynamics. The amount of crossing protein is quantified as the concentration of the cross-linker divided by the concentration of total actin ($R = [\alpha - actinin]/[actin]$) is varied in the range of 0-0.05.

Actin is key requirement for the function of living cells

Actin monomers polymerize in the presence of Mg^{2+} and ATP. The result of the process is a group of actin filaments that wrap together forming an entangled network.

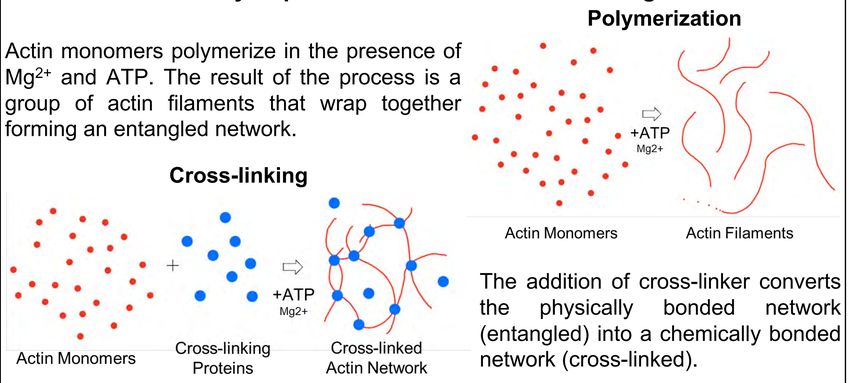

The addition of cross-linker converts the physically bonded network (entangled) into a chemically bonded network (cross-linked).

Figure 1: Sketches of actin polymerization and cross-linking. Exposure to certain environmental conditions (osmolarity, acidity, cross-linking molecules, etc.) will cause actin to reorganize into a variety of distinct networks. In this case the presence of magnesium will precipitate polymerization and α-actinin will cross-link the network.

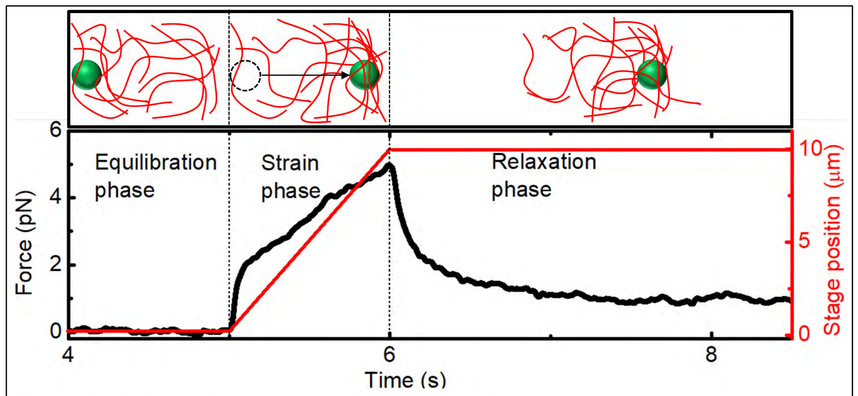

Figure 2: Schematics of a typical experimental setup.

- **Top panel:** Visual representation of the phenomena occurring in each of the three phases. Green sphere represents the microsphere, middle panel depicts the bead motion from left to right, network relaxation around the stationary bead.
- **Bottom Panel:** Trap position (red, right axis) and measured force (black, left axis) are shown for the three phases of the experiment: Equilibration, strain and relaxation. All the following results come from the strain & relaxation phases.

Cross-linking leads to increased network elasticity

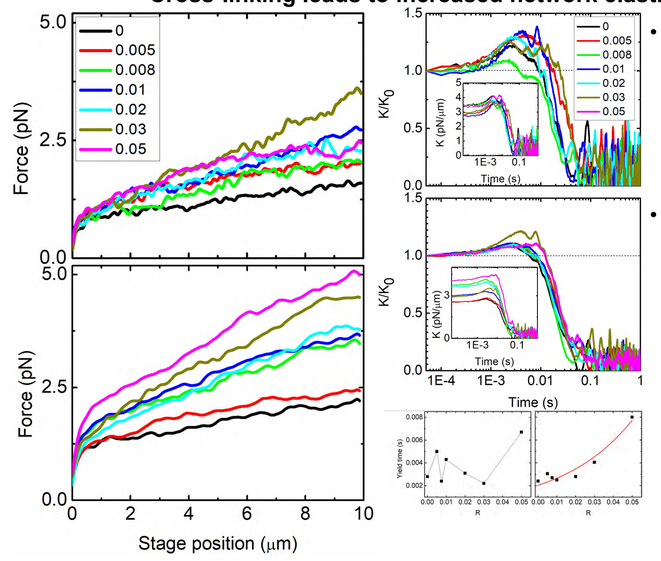

- **Left:** Response of the actin network during the strain phase at 5 (top) and 10 μm/s (bottom).
- **Right (top):** Normalized by k at t_0 (k_0) (main panel) and unnormalized (inset) differential moduli (dF/dx) of the forces shown on the left panels for 5 μm/s (top) and 10 μm/s (middle) speeds.

Figure 3: Strain force response. Right (bottom): Yield times as a function of cross-linker density. The yield time is when the maximum value of the differential modulus occurs. At the point, the actin transitions from elastic to plastic behavior and the network no longer exhibits a linear response on the stress/strain curve.

Relaxation mechanisms are affected by cross-linker concentration

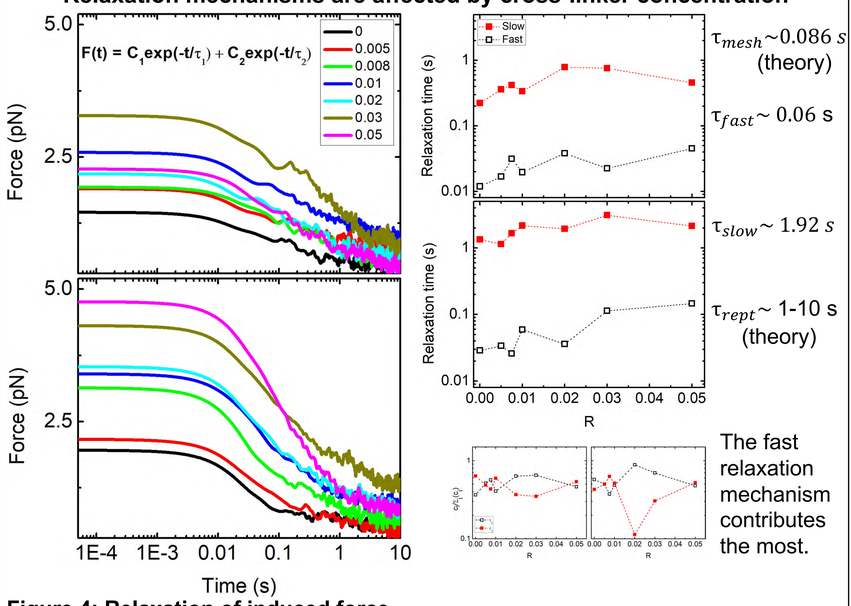

$\tau_{mesh} \sim 0.086\ s$ (theory)

$\tau_{fast} \sim 0.06$ s

$\tau_{slow} \sim 1.92\ s$

$\tau_{rept} \sim$ 1-10 s (theory)

The fast relaxation mechanism contributes the most.

Figure 4: Relaxation of induced force.

- **Left**: Response of the actin network during the relaxation phase.
- **Right top:** Relaxation times obtained from curve fitting to double exponential.
- **Right bottom:** Depict relative contribution of each (slow and fast) relaxation mechanism obtained from the fractional coefficients of each exponential terms. The fast relaxation mechanisms are represented in black.

Visible structural changes caused by α-actinin alter mechanical properties

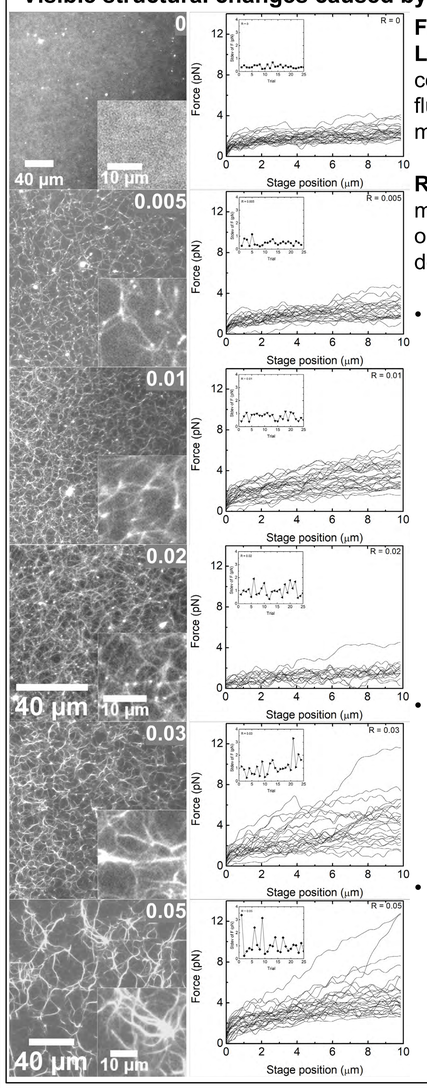

Figure 5: Structural evolution.

Left column: Z-projection of the 3D confocal microscopy images of the fluorescently labeled actin network with magnified overlay.

Right column: All of the 10 μm/s force measurements for the sample compiled into one graph with an inset of the standard deviation as a function of trial number.

- As the cross-linker ratio (displayed in top right corner of left column) increases visible structural changes become apparent. The network becomes bundled (thicker and brighter filaments) and the dynamics and mobility of the network decrease. This is because higher cross-linker ratios lead to more connections which create a stiffer network. Evidence for the decrease in mobility is seen by the increased sharpness each image displays. Less thermal motion allows for a sharper and more well-defined image to be captured.
- The heterogeneity of the network as the R value increases is displayed in the variable standard deviations across the trials. Image data also supports the increasing heterogeneity as more pockets of empty space appear as R increases.
- The denser and more bundled network appears to cause and increase in the force response of the network and additionally seems to increases the networks elasticity. This is supported by the increasing yield times and the larger for measurements obtained in the central panels.

Conclusions:

- Increasing the α-actinin to actin ratio of an actin network changes the structure of the network and alters the mechanical properties.
- All cross-linked networks exhibit substantial stress stiffening followed by softening at both speeds.
- Higher cross-linker density enhances the network connectivity that results in composites of isotropic filaments and bundles which also display increasing heterogeneity.

Acknowledgements:

- Bucknell Program for Undergraduate Research (PUR)
- Bucknell University Department of Physics and Astronomy

Ciprofloxacin accelerates gastrointestinal transit in a rodent model of FQAD

Jacqueline E. Kerler, Bitseat Getaneh, Eddie Lee, Cecilia Bove

Department of Biology, Bucknell University, Lewisburg, Pa.

Introduction

Fluoroquinolones (FQs) are an incredibly effective antibiotic meant to be prescribed for life-threatening conditions. However, they are often given for minor infections, which they should not be a treatment option for. Aside from this being problematic, the FDA has also warned that FQs can lead to a plethora of long-lasting and severe adverse side effect, described as Fluoroquinolone Associated Disability (FQAD).

Past studies have suggested that FQs may act as a selective inhibitor of $GABA_A$ receptors, keeping the inhibitory neurotransmitter GABA from binding in the central nervous system. GABA plays a key role in regulating the neural circuit that controls the vagus nerve by regulating the activity of the neurons of the Dorsal Motor Nucleus of the Vagus (DMV). The vagus nerve in turn modulates GI function via the vago-vagal reflex (Figure 1).

A potential consequence of this is gastrointestinal (GI) disease, due to how FQs may negatively modulate the vagus nerve. Preliminary data from our laboratory shows that patients that took FQs reported unwanted weight loss or gain, changes in appetite and motility disturbances, all of which could reflect dysfunctions of the vagus nerve.

The goal of this study was to assess whether or not ciprofloxacin (CPX), one of the most commonly prescribed FQ, could affect the vagus nerve in a rodent model. Specifically, we tested whether or not CPX would induce changes in body weight, appetite, and GI transit disturbances.

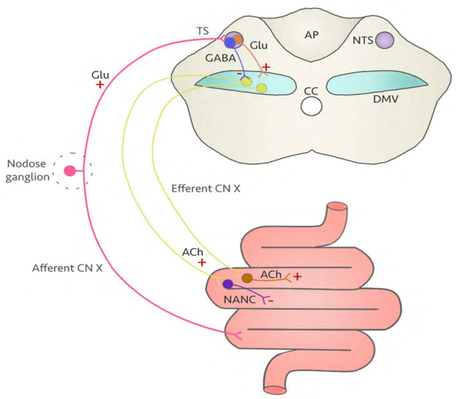

Figure 1: Schematic representation of the vago-vagal reflex. Image taken from Freeman M.Z. et *al.*, NeuroSci, 2021

Methods

Sprague Dawley rats were treated daily for 14 consecutive days with either 0.3ml of 0.9% saline (CTL) or 20 mg/kg of ciprofloxacin (CPX) via oral gavage. Weight changes and food intake were tracked daily. To test if digestion was affected, rats from both groups were fasted for 24 hrs and then treated with an oral gavage consisting of 1.5 ml of 0.5mg/kg of phenol red dye. After 20 minutes from the gavage, the rodents were sacrificed, and portions of the stomach, proximal, middle and distal small intestine were harvested, homogenized and the amount of dye recovered from these tissues was measured via spectrophotometry.

20 mg/kg CPX does not affect food intake and weight gain

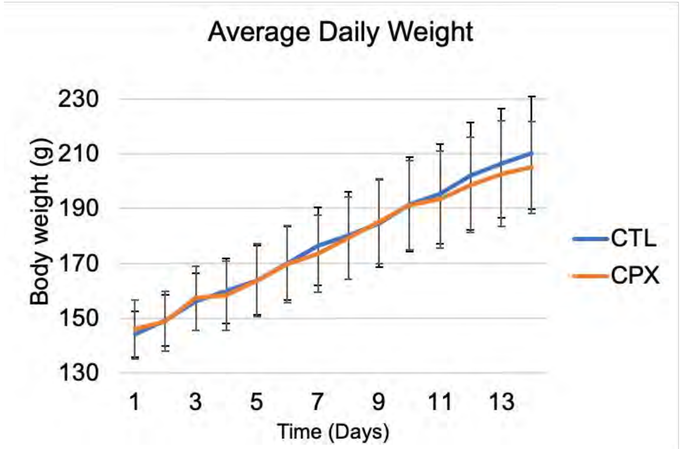

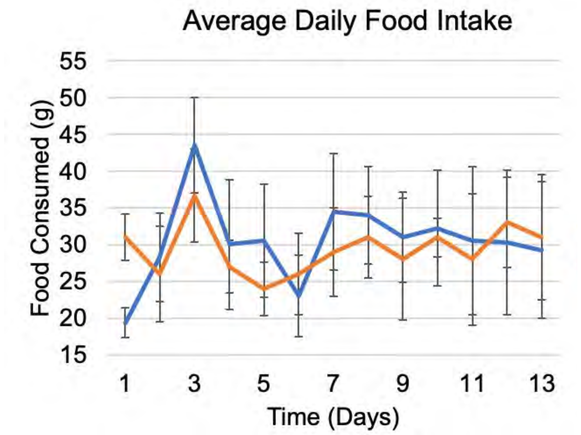

Left: Time course of weight gain during treatment with saline (CTL) or 20 mg/kg of CPX. Each line represents the average amount of weight gained by the two groups. No significant differences were found between CTL versus CPX, even when comparing males and females only (not shown; p>0.05).

Right: Line graph showing daily consumption of chow during the treatment period. Similar to the left panel, no significant differences were observed between CTL and CPX group (p>0.05). No significant differences when found when comparing the two groups according to the sex of the animal (not shown).

n=6 for both groups (3 males and 3 females in each)

20 mg/kg CPX significantly accelerates GI transit in females rats

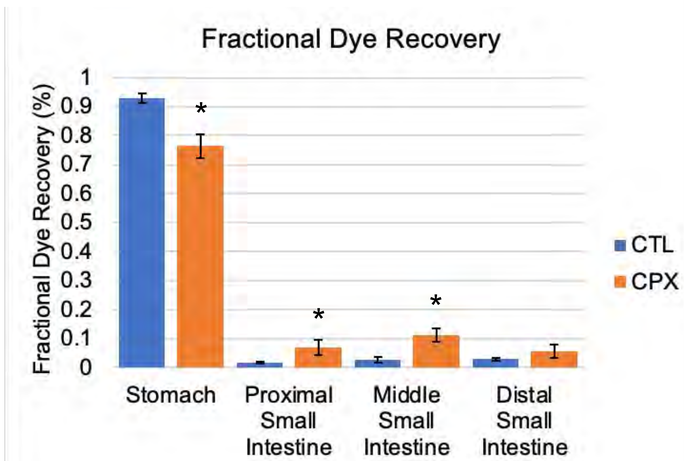

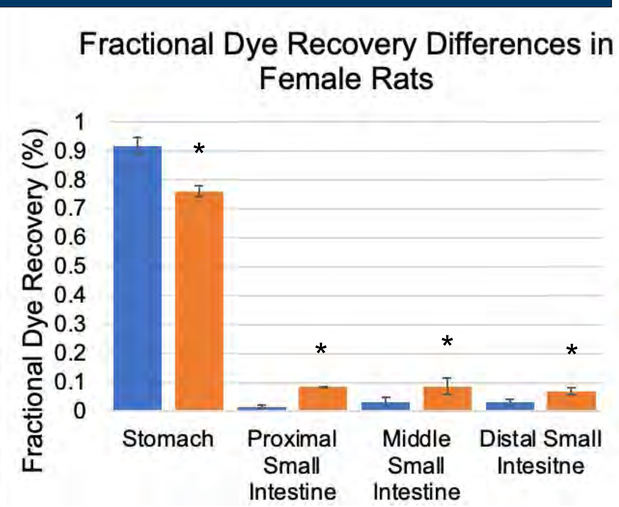

Left: Bar graph showing the percentage of dye recovered from the stomach, proximal, middle and distal small intestine of control rats (blue) and CPX treated rats (orange). There was significantly less dye recovered from the stomach of CPX-treated rats compared to CTL (76% versus 93% respectively), and more dye recovered from the proximal small intestine in the CPX group (6% versus 1% in CTL) and middle small intestine (11% versus 2% for CPX and CTL respectively), indicating that gastrointestinal motility is accelerated by CPX. n = 6 in both groups; * = p<0.05

Right: The amount of fractional dye recovery was significantly altered in female rats (n=3 in both groups) with the same trend observed when comparing the two treatment groups regardless of sex. While the same trend was also observed in male rats (n=3 in both groups; data not shown), there was no statistically significant difference in the amount of dye recovered in the GI tract, indicating that CPX is disproportionately affecting females over males. * = p<0.05

Discussion

While our preliminary study indicates that unwanted changes in body weight and appetite are reported by human patients following FQs administration, CPX did not affect weight gain nor the appetite of these rats at the dosage used. However, we were able to observe changes in gastrointestinal motility similar to those reported by our survey participants. This is suggesting that at the dose utilized in this study CPX is possibly inducing a gastrointestinal motility disorder. Since the transit is accelerated by CPX, it is likely that this drug is inhibiting the $GABA_A$ receptor at the level of the DMV, hence increasing the activity of these neurons. This might possibly dysregulate the vago-vagal reflex and the overall function of the vagus nerve. It is interesting to note that similar to human patients, female rats were more affected by CPX compared to males.

Conclusions

These results are strongly suggesting that CPX is inducing a functional gastrointestinal disorder in our experimental model. Further experiments are necessary to assess whether or not this increase in motility is due to changes in the activity of DMV neurons and whether or not the motor neurons within the myenteric plexus in the enteric nervous system are also affected. These results are providing further evidence of an additional permanent and long-lasting side effect of FQs administration that should be considered when prescribing these drugs to the general population.

References

1. Kabbani S. et *al.*, Clin. Infect. Dis. Off. Publ. Infect. Dis. Soc. Am. 2018
2. Yarrington M.E et *al.*, Infect. Control Hosp. Epidemiol. 2019
3. Halliwell R.F. et *al.*, J. Antimicrob. Chemother. 1993
4. Freeman M.Z. et *al.*, NeuroSci, 2021

Acknowledgments

This study is funded by the Biology Department at Bucknell University, Lewisburg, PA

BEEF LAB

Measuring Concordance of Sulcogyral Patterns in Monozygotic and Dizygotic Twin Pairs

Shane Kozick[2], Marisa Patti[1], Will Snyder[2], Donielle Beiler[1], Vanessa Troiani[1,2]

1. Autism & Developmental Medicine Institute, Geisinger Health System
2. Bucknell University

1 Background

- The brain's surface is made up of sulci (grooves) and gyri (ridges) that together create the distinct folded (sulcogyral) appearance of the brain.
- Alterations to the structure of the orbitofrontal cortex (OFC) have been linked to psychiatric disorders, including schizophrenia.
- Within the OFC, there is a high degree of individual complexity of folding. Four pattern types have been identified in the OFC based on the continuity of the medial orbital sulcus (MOS) and lateral orbital sulcus (LOS). See Figure 1.
- The spatial organization of these patterns are not identical in every individual that has the same overall pattern type. Rather, there are *subtypes* that can also be characterized within each pattern type.
- Monozygotic (MZ) twins are the same sex and share nearly 100% of genetic information. Dizygotic (DZ) twins can be the same or opposite sex and share approximately 50% of the same genes. Twin studies are useful for examining the role of genes in a trait or phenotype.
- Here, we complete the first characterization of twin OFC sulcogyral patterns, to understand their heritability.

Figure 1. Cartoon depiction of sulcal patterns.

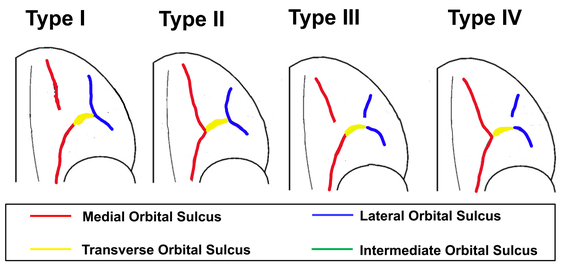

2 Methods

- Publicly available data from the Human Connectome Project for MZ and DZ twin structural MRI scans were processed through the automatic tracing pipeline.
- Anatomist, a neuroimaging software platform, was used to label the individual sulci fragments on both hemispheres of the brain (MOS, TOS, LOS, IOS).
- The labeled Anatomist image was uploaded to ITK-SNAP to display a color-coded, 3D image of the subject's OFC sulcogyral pattern.
- Two independent tracers identified the overall pattern type and then the subtype based on the orientation of the MOS, TOS, LOS, and IOS for both hemispheres of all subjects.

Table 1. Demographic Characteristics

Sample Demographics	Mean Age (SD)	Twin Pairs Total (% total)	Mean BMI (SD)	Mean Height (SD)
MZ	29.4 (3.3)	148 (63.9%)	26.3 (4.7)	67.0 (3.7)
DZ	29.1 (3.6)	81 (36.1%)	26.3 (5.4)	67.7 (3.7)
Sex	**MZ**	**% of Total**	**DZ**	**% of Total**
Male	58	25.2%	29	13.9%
Female	90	38.7%	52	22.3%

3 Results

Figure 2. Frequency Distribution of Pattern Types in MZ and DZ Twins

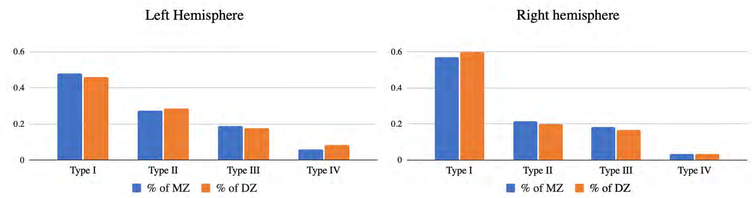

Figure 3. Concordance of Overall Pattern Types

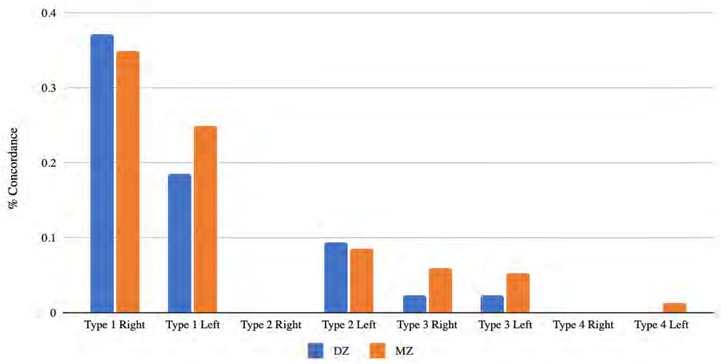

Figure 4. Cartoon depiction of example pattern subtypes for Type I patterns.

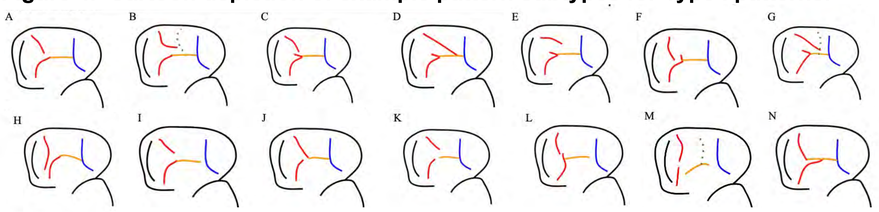

Figure 5. Sulcogyral Pattern Subtype Variation for All Subjects

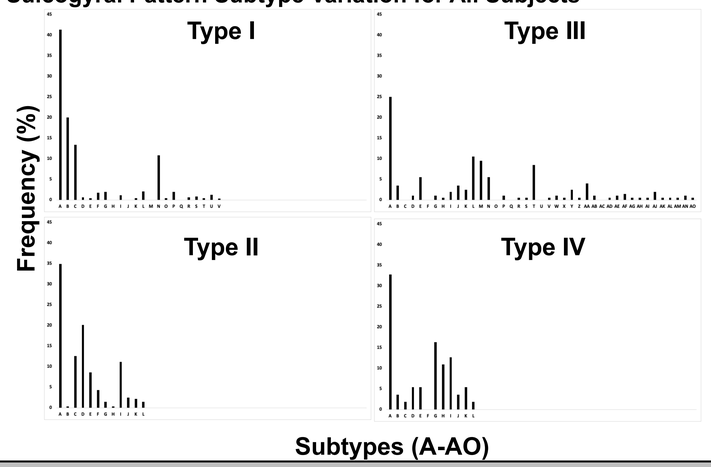

4 Results

Figure 6. Radial Plot of Novel Type I Pattern Subtypes

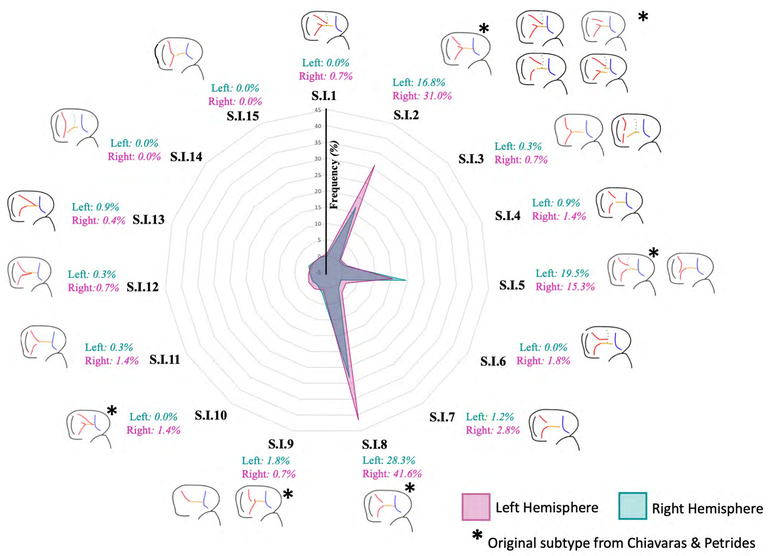

- Distinct features of each pattern subtype were described and each subtype was coded as a unique vector based on the presence or absence of these features.
- Principal Components Analysis was run to identify components that explain the most variance.
- Radial plot depicts the frequency of individual subtypes across all twins, by hemisphere, with subtypes that are clustered together based on PCA.

5 Conclusions & Future Directions

- These results are the first examining OFC sulcogyral pattern distributions in MZ and DZ twins.
- We find similar overall frequency distributions for pattern Types I-IV.
- OFC sulcogyral patterns may capture important variance that is not genetic in origin but is relevant to psychiatric disease risk.
- We identified a large number of pattern subtypes that have not previously been described. Analyses with pattern subtypes are ongoing and indicate potentially novel ways to group pattern subtypes.

6 References

1. Chiavaras MM, Petrides M. Orbitofrontal sulci of the human and macaque monkey brain. The Journal of Comparative Neurology. 2000;422(1):35–54.
2. Patti, M. A., & Troiani, V. (2018). Orbitofrontal sulcogyral morphology is a transdiagnostic indicator of brain dysfunction. Neuroimage Clin, 17, 910-917.
3. Snyder, W., Patti, M., & Troiani, V. (2019). An evaluation of automated tracing for orbitofrontal cortex sulcogyral pattern typing. Journal of neuroscience methods, 326, 108386.

Structure-Function Relationship of Musculoskeletal Microstructure

[1]Minhaj Bhuiyan, [2]Jaden Lee, [2]Sabrina Lorza, [2]Prof. Benjamin Wheatley
[1]Biomedical Engineering Department, Bucknell University, Lewisburg, PA
[2]Mechanical Engineering Department Bucknell University, Lewisburg, PA

Bucknell University
Mechanics and Modeling of Orthopedic Tissues

INTRODUCTION

- Skeletal muscle is responsible for essential functions such as breathing and locomotion.
- Complications such as sarcopenia, pressure ulcers [2], and cerebral palsy arise with aging [1].
- Understanding the structure-property relationship of muscle tissue will enhance clinical practice.

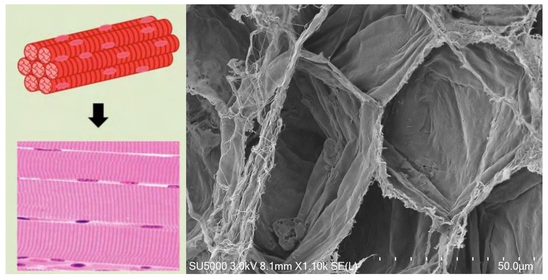

FIgure 1: Depiction of muscle fibers and extracellular matrix.

HYPOTHESES

1) Biaxially stretched tissue will be significantly stiffer than uniaxially stretched tissue
2) There is a direct correlation between intramuscular pressure and compressive loads
3) Tension-compression asymmetry can be modeled via a Von Mises bivariate fiber distribution

OBJECTIVES

To study the *structure-function relationship* in muscle tissue via:

1) Multiaxial tensile testing
2) Uniaxial compressive testing
3) Multiscale finite element modeling.

METHODS

EXPERIMENTALLY:

1) Harvest fresh porcine hind limb from George Farms
2) Follow standard dissection procedure to prepare specimens for biaxial tensile and uniaxial compressive testing
3) Process DIC and intramuscular pressure data in *VIC2D* and *MATLAB*, respectively

Figure 2: Porcine hind limb

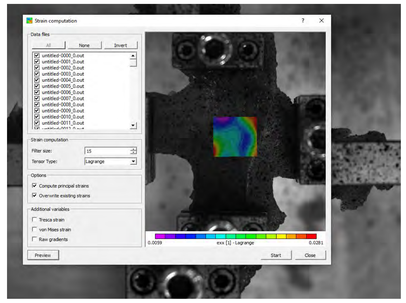

Figure 3: DIC data acquisition.

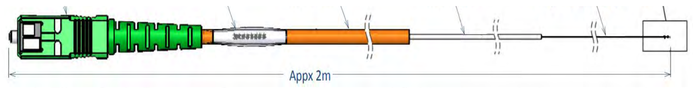

Figure 4: Fiber Optic Pressure Sensor used to record fluid pressure during compression testing.

COMPUTATIONALLY:

1) Generate a muscle tissue geometry using open source plugin *GIBBON-Code*
2) Apply biaxial tension and compression boundary conditions in finite element package *FEBio*
3) Run a monte carlo simulation with latin hyper-cube sampling in *MATLAB*

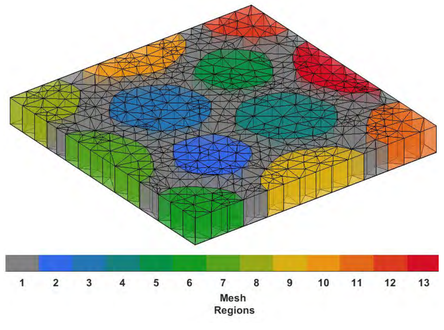

Figure 5: *GIBBONCode*-generated of representative muscle tissue geometry

RESULTS

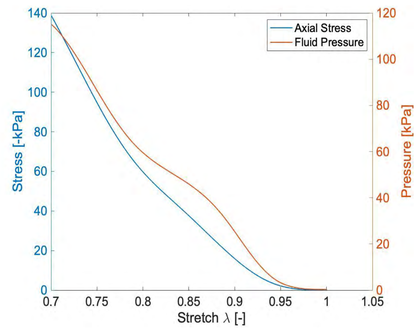

Figure 6: Stretch-stress and pressure-stretch curves for cubic muscle specimen compressed uniaxially.

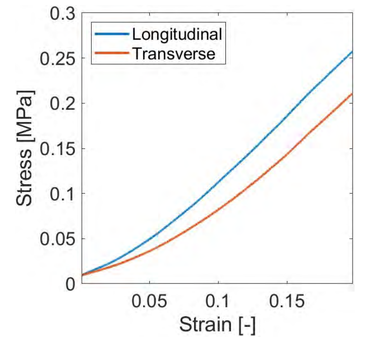

Figure 7: Stress-strain curves for cruciform muscle specimen stretched in longitudinal and transverse direction relative to fibers.

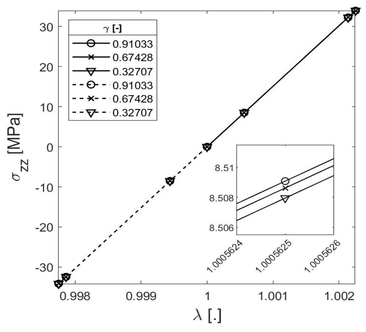

Figure 8: Stress-stretch curves for muscle stretched transversely where cosine of gamma is set to 0.91033, 0.67424, and 0.3. The embedded curve depicts variance between the three curves.

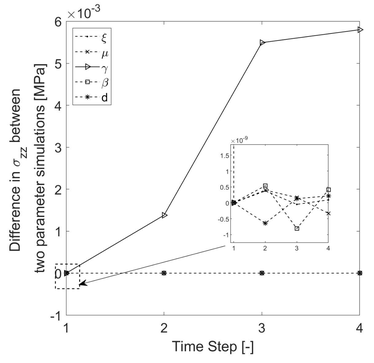

Figure 9: Curves depicting stress calculation differences between using gamma 0.91033 and 0.6724 per time step. The embedded curve depicts sensitivity in von Mises parameters xi, mu, beta, and d.

FUTURE WORK

1) Calculate and determine statistical significance of elastic moduli of transverse and longitudinal stress-strain curves.
2) Implement intramuscular pressure data into a finite element model
3) Submit computational results for review in *Computer Methods in Biomechanics and Biomedical Engineering*

SUMMARY & CONCLUSIONS

- **Compression of skeletal muscle tissue affects fluid pressure.**
- **There is a significant difference in stiffness based on the direction of stretch of the skeletal muscle.**

ACKNOWLEDGMENTS

1) Clare Boothe Luce Foundation
2) Costa Healthcare Fund
3) John P and Mary Jane Swanson Professorship

REFERENCES

[1] Wheatley, B. B. (2020). Investigating Passive Muscle Mechanics With Biaxial Stretch. Frontiers in Physiology, 11, 1021. https://doi.org/10.3389/fphys.2020.01021
[2] Lavigne, T., et al. Poro-Elasticity Is Able to Capture the Apparent Viscoelastic Behaviour of Passive Muscle in Confined Compression. p. 35.

Nutrient Availability Determines Colony Morphology in a Two-Species Cross-Feeding System: Simulation and Analysis

Jiaqi Lin[1], Paul Sun[2], Jiajia Dong[3]

1 Department of Computer Science & Engineering, Bucknell University, Lewisburg, PA, 2 Applied Math, California State University, Long Beach, CA, 3 Department of Physics & Astronomy, Bucknell University, Lewisburg, PA,

Introduction

One of the outstanding questions in ecology is species diversity. Inspired by the observation of bacteria coexisting in a community, we explore the emergence of spatial structure given a simple cross-feeding mechanism between two species. By studying these patterns, we investigate the interaction between two species.

Cross-feeding Model

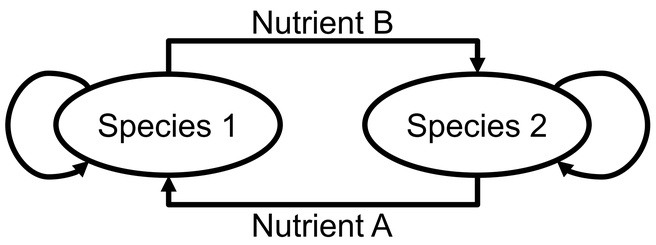

Fig. 1 One species produces nutrients that are essential for the other, and vice-versa.

- Agent-based model for 2D square lattice, where each lattice site occupied by at most one species.
- Kinetic Monte Carlo algorithm to simulate cross-feeding mechanism: species division, species take up, species excretion, and nutrient diffusion.

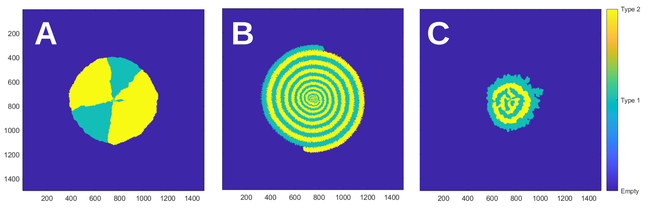

Fig. 2 Various colony morphological examples. (A) Sectors occurs with universally placed nutrients; **(B)** Spiral Pattern, and **(C)** Engulfment pattern occurs randomly without universally placed nutrients..

Method

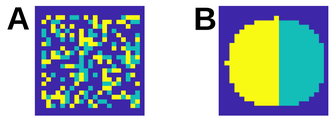

Fig. 3 Two Initial Conditions Used in Simulation. (A) Randomly placed equal number of two types of bacteria into a square box in the center of lattice **(B)** Separately place bacteria into two halves of a circle in the center of lattice

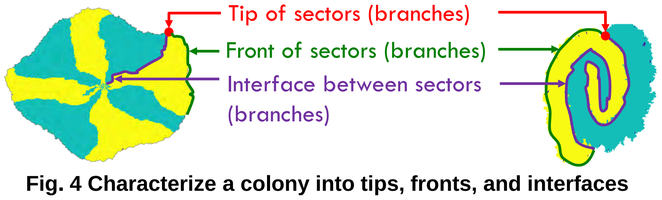

Fig. 4 Characterize a colony into tips, fronts, and interfaces

Results

Upper Tip / Lower Tip	Left	Right	Up
Left	Engulfing	Spiral	Unknown
Right	Spiral	Engulfing	Unknown
Down	Unknown	Unknown	Elongated

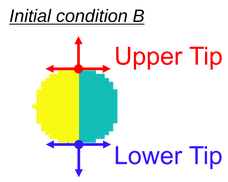

Fig. 5 Colony Morphology with Two Tips. This chart summarizes morphologies emerge starting from a simple separated initial conditions, analyzing through movement of tips at the colony.

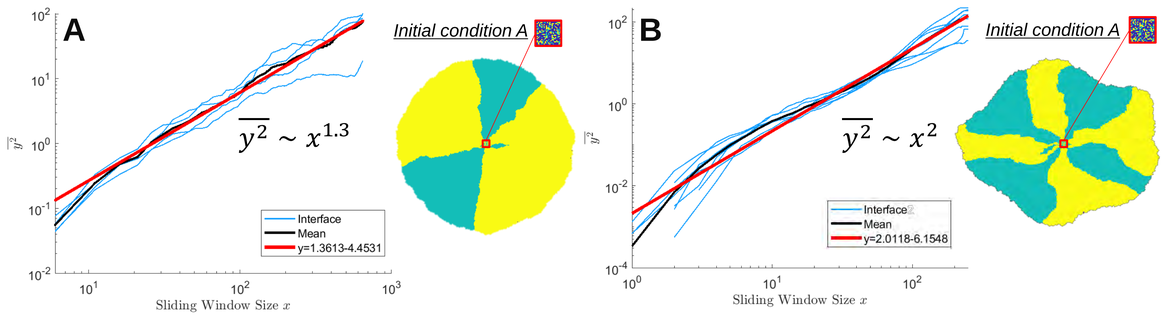

Fig. 6 [Sector] Measurements on Fluctuation of Interface[1]. All interfaces of sectors for colony initialized universally placed nutrients and without initial nutrients is measured. **(A)** Colony with universally placed nutrients shows a smoother fluctuation, indicating a more stable pattern (See **Fig. 4A**). **(B)** In contrast, without universally placed nutrients, colony is prone to transformed into a spiral patter (See **Fig. 4B**).

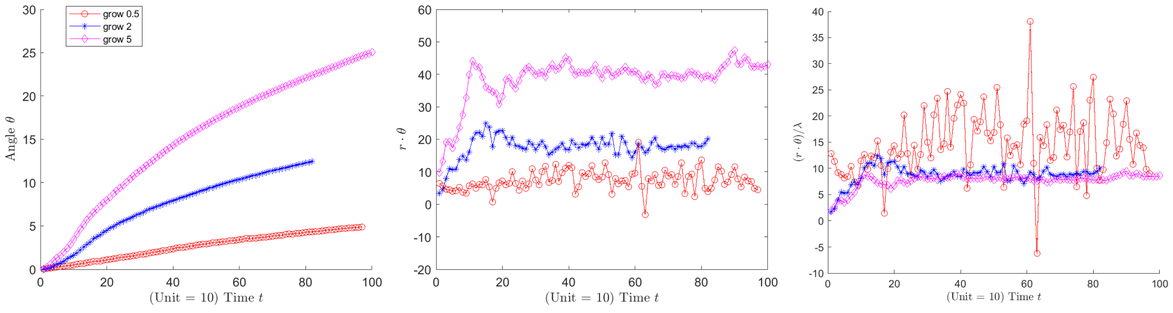

Fig. 7 [Spiral] Increment in radius and angle scaled with growth rate in low nutrient-diffusion rate mode. θ is the angle of tip indicating the rotation; r is the radius from the center to tip; and λ is the bacteria growth rate. When nutrients diffuse slowly, adjusting in growth rate contributes to the speed of formation of colony.

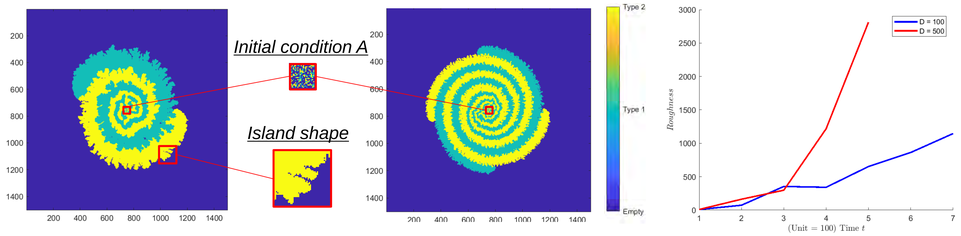

(a) $D = 500$ (b) $D = 100$ (c) Roughness Vs. Time

Fig. 8 [Spiral] At high growth rate, higher nutrient diffusion rate, D promotes roughness of front of colony. At high diffusion rate, the boundary of colony forms island-like pattern .

Conclusion

- When nutrients are abundant, the colony expands as the two species grow in radial sectors. (See **Fig. 4A** and **Fig. 7**).
- When nutrients become limiting, the two species grow along an interface, resulting in a spiral pattern (See **Fig. 4B** and **Fig. 7**).
- Transformation from radial growth into spiral growth is signified by the annihilation between two neighboring tips.
- Once this transformation is done, the colony pattern is stick to a certain type.
- Nutrient diffusion plays a crucial role in the colony pattern as well as the coexistence of the two species.

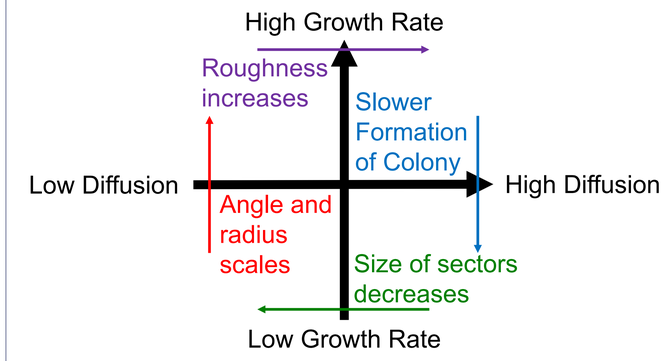

Fig. 9 Effects of tuning nutrient diffusion rate and cell growth rate.

Future Work

- With high nutrient diffusion, the colony formed sectors before emergence of spiral pattern. Thus, a matrix to detect the size of these sectors size is needed to understand the cause of various sector size.
- Contribution of other parameters to the morphologies of colony, such as toxicity, nutrient execration rate etc.

Reference

[1] Oskar Hallatschek, Pascal Hersen, Sharad Ramanathan, and David R. Nelson. Genetic drift at expanding frontiers promotes gene segregation. Proceedings of the National Academy of Sciences, 104(50):19926–19930, 2007

Acknowledgement

This research is funded by:
NSF through grants DMR-1703231 and MCB-2029480.

Solanum 'Deaf Adder', a New Bush Tomato Species from the Australian Monsoon Tropics

Figure 1 *Solanum* sp. 'Deaf Adder' in its natural habitat. Photo by Kym G. Brennan

Based on its geography and unique morphological characteristics, the 'Deaf Adder' bush tomato is a distinct species.

Claire E. Marino[1], Tanisha M. Williams[1], Christopher T. Martine[1]
[1]Bucknell University Department of Biology, 1 Dent Drive, Lewisburg, PA 17837

Project Goal

To describe and classify *Solanum* sp. 'Deaf Adder' as a new species by measuring morphological characteristics and using data analyses to compare its features to those of its close relatives *Solanum asymmetriphyllum* and *Solanum sejunctum*, effectively introducing it to the scientific community.

Background

Australia is a unique island continent with a wealth of endemic species, many of which are waiting to be introduced to the scientific community— as of 2009, there were 147,579 accepted described species in Australia. This seems like a lot, but there is an estimated total of 566,398 species in Australia, meaning that over 70% of species on the continent have yet to be described (Chapman, 2009). Kakadu National Park, which consists of almost twenty thousand square kilometers, is a particularly biodiverse area within northern Australia. Common terrain types include lowlands, plateaus, and floodplains, occurring in a monsoonal climate in which the wet season occurs October through March (Banfai & Bowman, 2007). The park hosts a number of endemic *Solanum* species, including *S. ultraspinosum* A.R. Bean, *S. clarkiae* Symon*, S. sejunctum* K. Brennan, C. Martine, & Symon, and *S. asymmetriphyllum* Specht (Bean, 2016; Martine et al. 2019). *Solanum* sp. 'Deaf Adder' has been suggested by regional botanists to be a localized variant of *Solanum asymmetriphyllum*, a functionally dioecious species (Symon,1981) that is widespread in the escarpment region of Kakadu. *Solanum* sp. 'Deaf Adder' appears to be limited to Deaf Adder Gorge, a remote area in the southern part of the park - and is similar in its limited distribution to *Solanum sejunctum,* another localized variant that was segregated from *S. asymmetriphyllum* in 2006 (Brennan et. al, 2006). This study seeks to measure and compare morphological differences between the three taxa to determine whether *Solanum* sp. 'Deaf Adder' should be considered a distinct species (Figure 2).

Methods

- Measurements were taken from a single female *Solanum* sp. 'Deaf Adder' plant. It is the only specimen cultivated in Bucknell's Burpee Greenhouse, and happens to be the only specimen being cultivated outside of its natural habitat.
- Measurements were taken using a dial caliper and/or tape measure.
- Measurements included but were not limited to: prickle density on calyxes, leaves, and stems; fruit diameter and height; fruit wall width; seed number and length; leaf asymmetry and length; et cetera. The expected number of analyzed traits is a minimum of 34.
- Features such as leaf area were processed via ImageJ.
- Principal components analysis (PCA), analysis of variance (ANOVA), and post-hoc testing will be performed to evaluate the significance of the characteristics of *Solanum* sp. 'Deaf Adder' compared to *Solanum sejunctum* and *Solanum asymmetriphyllum.*
- We will then designate a Latin name for the species.

Morphometric Results

- Based on the morphological measurements used in this analysis (*N* = 13 traits) there is clear separation and strong evidence to support that *Solanum* sp. 'Deaf Adder' is its own species (Figure 4).
- The first two axes of the PCA analysis explained 65.5% of the variation (Figure 4).
- The ANOVA tests confirmed that the morphological characters were different among the three species. Ten of the 13 traits were statistically significant (all $P < 0.001$).

Figure 2. Flowers, flower calyxes, and leaves of *Solanum* sp. 'Deaf Adder' (center column) next to *S. asymmetriphyllum* (left) and *S. sejunctum* (right).

Journey to Bucknell

The *Solanum* sp. 'Deaf Adder' specimen here at Bucknell is the only specimen growing outside of Deaf Adder Gorge. Ten seeds from a female specimen collected in 2006 by K. G. Brennan located at the Northern Territory Herbarium in Australia (Figure 3) were brought back to Bucknell by Dr. Chris Martine in 2018. Of those seeds, four germinated, and only one survived.

Figure 3. 2006 Female *Solanum* sp. 'Deaf Adder' specimen collected by Kym G. Brennan from the Northern Territory Herbarium.

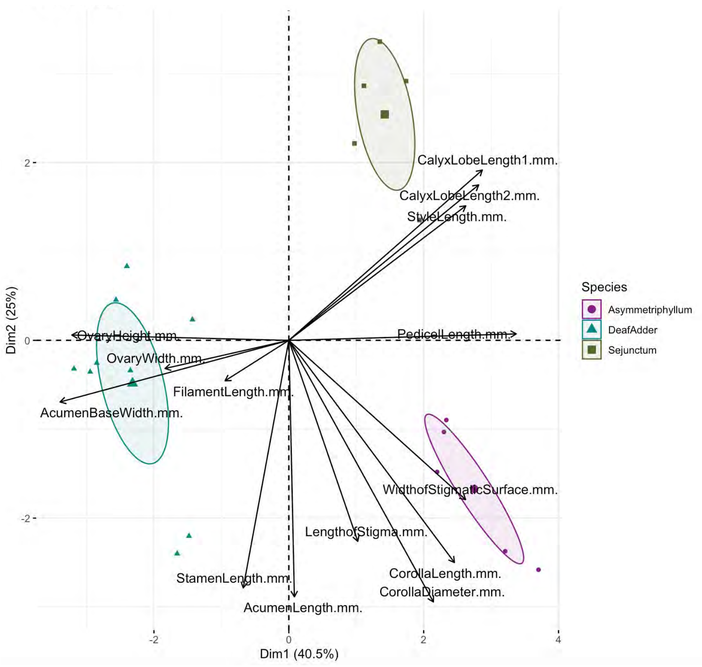

Figure 4. Principal components analysis (PCA) of the 13 morphological traits of the three *Solanum* species. Biplot shows PC1 versus PC2, which explains 65.5% of the variation.

Funding and support generously provided by the David Burpee Research Fund, the Manning Internship in Botanical Science, and the Bucknell Department of Biology, and the Wayne Manning Internship Fund.

Special thanks to K. G. Brennan (for making the collection from which seeds were removed and for providing the only known field photo), Angela McDonnell, Peter Jobson, and the staff of the NT Herbarium at Darwin.

Bucknell UNIVERSITY BIOLOGY DEPARTMENT

References

Banfai, Daniel S., & Bowman, David M. J. S. (2007). Drivers of Rain-Forest Boundary Dynamics in Kakadu National Park, Northern Australia: A Field Assessment. *Journal of Tropical Ecology, 23*(1), 73-86.

Bean, A. (2016). Two new species of Solanum (Solanaceae) from the Northern Territory, Australia. *Austrobaileya*, 9(4), 524-533. Brennan, K., Martine, C. T., & Symon, D. (2006). 'Solanum sejunctum'(solanaceae), a new functionally dioecious species from Kakadu National Park, Northern Territory, Australia. *Beagle: Records of the Museums and Art Galleries of the Northern Territory,* 22, 1-7.

Chapman, A.D., 2009. Numbers of living species in Australia and the world.

Symon, D. E. (1981). A revision of the genus Solanum in Australia. *Journal of the Adelaide Botanic Gardens* 4: 1–367.

Martine, C.T., I.E. Jordon-Thaden, A.J. McDonnell, J. Cantley, D. Hayes, M. Roche, E.S. Frawley, I.S. Gilman and D. Tank. 2019. Phylogeny of the Australian *Solanum dioicum* group using seven nuclear genes: Testing Symon's fruit and seed dispersal hypotheses. *PLoS ONE* 14(4): e0207564.

Regional and racial/ethnic disparities in state-level use for lisdexamfetamine (Vyvanse) amidst the COVID-19 pandemic

AnnMarie N. Onwuka[a†], Johanna A. Arevalo[b‡], Vanessa N. Bueno[a‡], Jaeger K. Kubikisha[c‡], Angelique L. Starke[d‡], Janet Suarez[c‡], Kenneth L. McCall[f], Brian J. Piper[c]
[a]University of Scranton, [b]University of Pittsburgh, [c]Geisinger Commonwealth School of Medicine, [d]Temple University, [e]Swarthmore College, [f]University of New England

Background

- Rising number of prescriptions for Attention Deficit Hyperactivity Disorder (ADHD) medications is disproportionate amongst lower income areas.
- Our goal was to investigate current trends in lisdexamfetamine (LDX) prescriptions across the US.
- COVID-19 may have impacted these trends.

Methods

- Collected national and statewide data for LDX prescriptions using Medicaid, the Automation of Reports and Consolidated Orders System (ARCOS), and the American Community Survey.
- Completed correlations between LDX prescriptions and race/ethnicity demographics per state.

In the US, there were **regional and racial/ethnic disparities** in the distribution of **lisdexamfetamine**, a medication used to treat ADHD and BED.

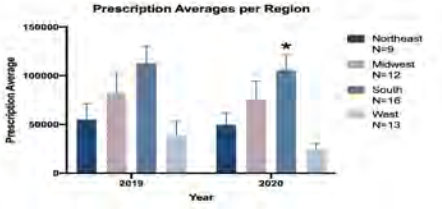

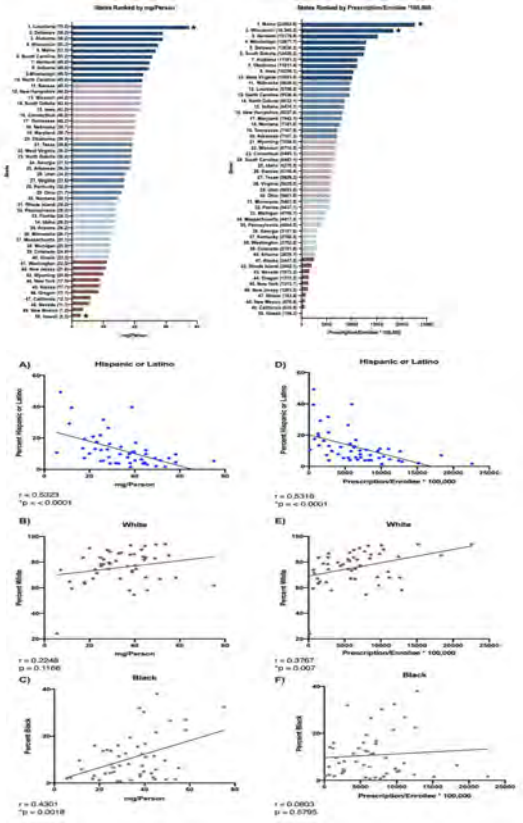

Results

- Q2 and Q4 had significant differences in their LDX prescriptions from 2019-2020.
- The South had the highest number of prescriptions and mg/person, and the most significant change during COVID-19.
- Hispanic/Latino populations had strong negative association with LDX distribution.

Discussion

- There were regional and racial/ethnic disparities that still must be addressed.
- Further research could look at other marginalized populations.
- Change in prescriptions between 2019 and 2020 could be attributable to the COVID-19 pandemic.

Limitations

- Replaced missing 2020 data from Medicaid with 2019 data.
- Unable to account for independent insurers.

Trajectory Gaze Path Analysis and Isolating Areas of Interest in Eye-Tracking Data for Autism Spectrum Disorder Studies

Kartikeya Sharma, Dr. Brian King, Dr. Vanessa Troiani

Geisinger Autism & Developmental Medicine Institute (ADMI), Lewisburg, PA

Department of Computer Science, Bucknell University, Lewisburg, PA

Context

According to the CDC, about 1 in 59 children have autism spectrum disorder or ASD, representing a significant percentage of the population.[2] Unfortunately, this condition often remains undiagnosed until later in childhood, which, in turn, delays many clinical treatments that could improve social functioning outcomes.

Previous research in ASD has leveraged both computer hardware and software to assess how visual attention differs between neurotypical subjects against those subjects diagnosed with ASD. Eye-tracking technology has been at the forefront of research in this area.

A standard experimental setup in ASD research employs static stimuli that contain a spatially separated set of objects (e.g., Figure 1A). Researchers present a subject with a stimulus, and eye-tracking systems record their gaze over a short, fixed period of time.

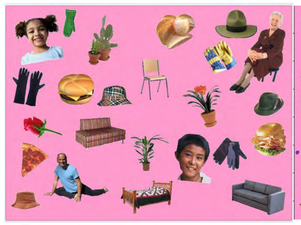

Figure 1A. An array of stimuli, including photos of social and inanimate objects [1]

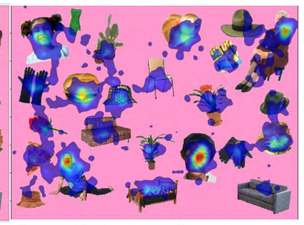

Figure 1B. Similar to Figure 1A with an overlaid heat map intensely coloring objects that were focused on for more extended time [1]

ASD experts have found that neurotypical children generally focus more on social images, such as those of people or food, than on pictures of inanimate objects. In contrast, children with ASD tend to show no preference for social over non-social stimuli. Researchers in these clinical settings have also summarized eye-tracking data using a heat map, highlighting how long participants in both groups have looked at a given stimulus. However, heat maps (shown in Figure 1B) forgo clinically crucial information about how children cognitively prioritize stimuli over time.

Objectives

Eye-tracking analysis software packages are available that analyze eye-tracking data. However, most of these applications perform aggregate analyses that discard valuable temporal information contained in these data.

Our work aims to provide a publicly available software application for eye tracking researchers that provides:

- Support for standard Tobii eye-tracking systems and data
- Support for standard preprocessing filters and visualizations for eye-tracking data, including scatter plots, gaze paths, fixation plots, and heat maps
- Access to novel methods under development that provide new techniques to identify and visualize gaze patterns from large cohort eye-tracking studies

Methods and Results

Building upon prior research from Dr. Brian King and Dr. Vanessa Troiani, our work focuses on:

- Data mining and machine learning techniques for the identification of frequently-occurring gaze paths among multiple participants viewing identical stimuli
- Machine learning techniques to aid classifying and categorizing underlying areas of interest
- Software frameworks to support the design and development of a modern eye-tracking analysis application with emphasis on usability

Machine learning for frequent gaze path identification

Identifying frequent gaze paths requires clustering fixations over multiple participants. The resulting clusters contain fixations from many participants suggest that multiple participants had similar interests. Such clusters of fixations become candidates for frequently-occurring gaze paths of interest. Clusters are identified, labeled, resulting in each gaze path. The application then transforms the clusters into a simple sequence of cluster identifiers. Much of the initial part of this research has focused on evaluating clustering techniques that correctly identify clusters over areas of interest while eliminating outlier fixations in a cluster.

Density-based clustering techniques are well-suited in distinguishing clustered points from outliers. Data scientists use the OPTICS and DBSCAN algorithms for this purpose.

Deep learning for automated Area of Interest (AOI) analysis

It is of great interest to researchers to understand the type of objects that are drawing significant attention from multiple participants. We have begun work that uses convolutional neural networks to 1) automatically identify AOIs in a stimulus, and 2) classify and label AOIs to determine the type of object of interest.

Python for Application Development

The data visualization algorithms are accessible to end-users through an interactive graphical user interface (GUI) encapsulated within a software toolkit. The toolkit can view gaze or fixation data across a selected set of participants for a particular stimulus via the following types of plots: scatter plot, line plot, heatmap, and clustering. By and large, the project, developed in Python, uses pandas for data import, selection, preprocessing, NumPy for algorithmic and arithmetic computations, PyQt5 for the graphical user interface, and Plotly as an interactive, visually advanced plotting backend embedded within the PyQt5 application.

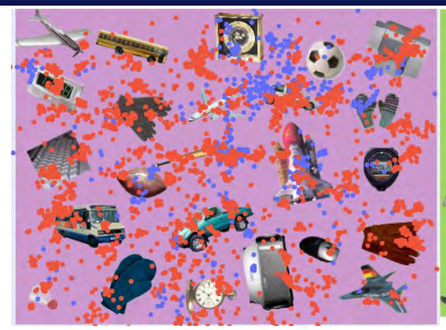

Figure 2. Scatter plot of two participants looking at a stimulus with each color representing a particular participant. The application developed in this research produced this scatter plot.

Figure 3. Cluster plot (using OPTICS algorithm) depicting a participant looking at a stimulus, where each color represents a cluster. The application developed in this research produced this cluster plot.

Figure 4. Leveraging a pre-trained convolutional neural network to identify and label objects within a stimulus with the associated percentage of confidences for each label.

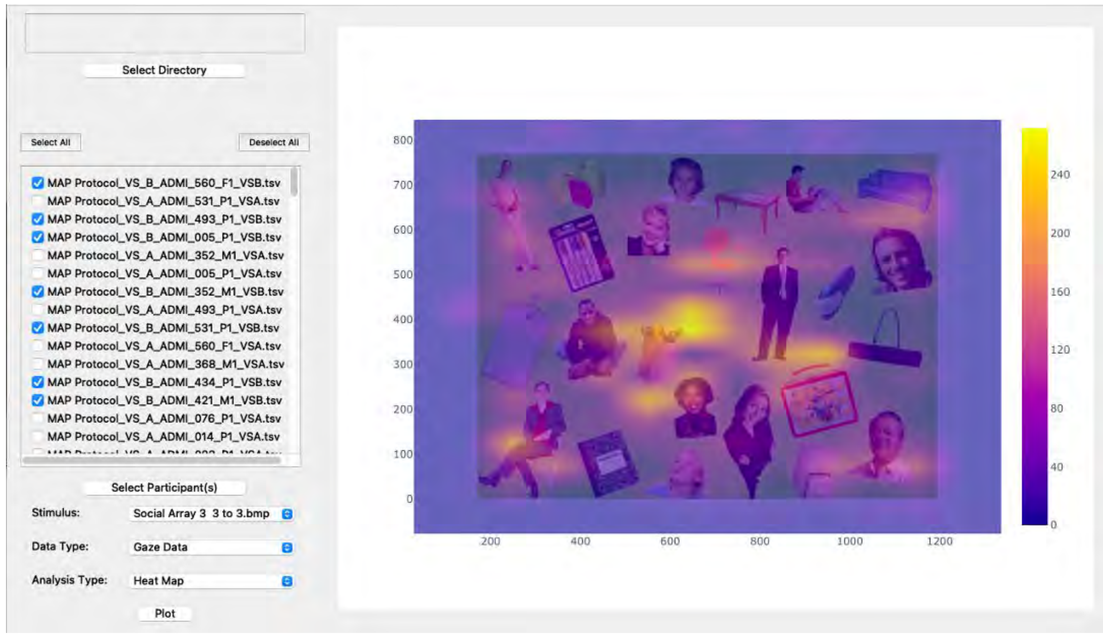

Figure 5. Smoothed and alpha-blended heatmap of multiple participants looking at a stimulus with the warm intensity of the color representing the amount of eye-tracking points concentrated at a particular region. The application developed in this research produced this heatmap.

Future Work

Work is currently progressing on the application. We are working to address:

- **Improved clustering that eliminates parameter selection** - Further work is currently underway to provide an estimation of a reasonable number of points per cluster suggested to the end-user for a particular data set.
- **AOI classification** - Development of convolutional neural network to classify areas of interest with many fixations.
- **Open-source release of application** - Open-source publishing of application on GitHub for fellow eye-tracking data researchers, including autism spectrum disorder researchers working with eye-tracking data

Conclusion

Upon full completion of our software development and release under open-source licensure, ASD researchers will be able to view eye-tracking data in both an aggregate and temporal way and define areas of interest, i.e., foci in the images, while also providing researchers with animated plots to provide temporal visualizations of the gaze or fixation eye-tracking data. Ultimately, the eye-tracking models created by ASD researchers with our toolkit will, downstream, aid in earlier diagnosis and better social outcomes for those with ASD.

Selected References

1. Sasson, N. J., Turner-Brown, L. M., Holtzclaw, T. N., Lam, K. S., & Bodfish, J. W. (2008). Children with autism demonstrate circumscribed attention during passive viewing of complex social and nonsocial picture arrays. *Autism Research*, *1*(1), 31-42.
2. U.S. Department of Health & Human Services.Data & statistics on autism spectrum disorder. Retrieved from https://www.cdc.gov/ncbddd/autism/data.html

Acknowledgements

I want to thank Dr. Vanessa Troiani from Geisinger's Autism & Developmental Medicine Institute (ADMI) and Dr. Brian King from Bucknell University for their guidance throughout this research project.

Chemical and Nanomechanical Analysis of Cat and Rat Whiskers

Davin Sim[1], Donna Ebenstein[1]

[1]Biomedical Engineering Department, Bucknell University

INTRODUCTION

- Cats use their whiskers to hunt for food, while rats use their whiskers more actively to navigate in tight dark spaces (Figure 1)
- Cat whiskers have larger diameters than rat whiskers, and the cat center (medulla) is filled compared to the rat medulla which is hollow (Figure 2)
- Most studies have focused on whisker sensing mechanisms [1], rather than the structure of the whiskers themselves
- A systematic study of whiskers will contribute to future design of biomimetic whiskers for sensing robots such as NASA's Curiosity rover [2]
- **Goal of the Project:** To perform a chemical and nanomechanical study of rat and cat whiskers to investigate trends in their structures or properties based on how each whisker is used

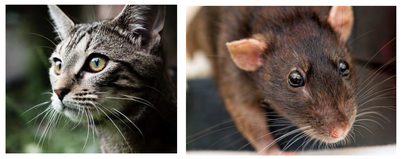

Figure 1: Images of (a) cat and (b) rat whiskers.

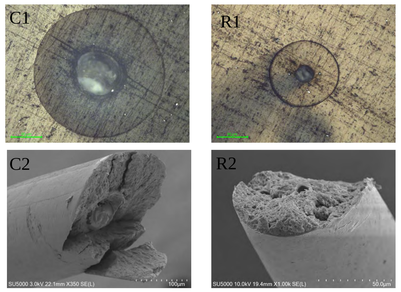

Figure 2: Optical microscope images of transverse sections of cat (C1) and rat (R1) whiskers. SEM images of fractured cat (C2) and rat (R2) whiskers.

METHODS

Sample Preparation

- Cat and rat whiskers were embedded in an epoxy resin (Figure 4) and polished manually down to 1200 grit to reveal transverse sections (Figure 2) or longitudinal sections (Figure 4)
- Embedded whiskers were analyzed using μRaman spectroscopy and nanoindentation

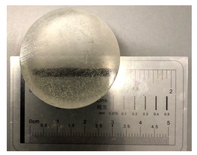

Figure 4: The epoxy resin with embedded whiskers.

Raman Spectroscopy

- μRaman spectrometry provides a chemical fingerprint of the proteins in the whiskers
- A HORIBA Xplora PLUS spectrometer with as 785-nm laser at 100x magnification was used to minimize background fluorescence
- Spectra collected with a 30-s acquisition time within the range of 400-3400 cm^{-1} following a 30-s delay
- Peak locations for each spectra were compared to published values for pure keratin [3] (Figure 5)

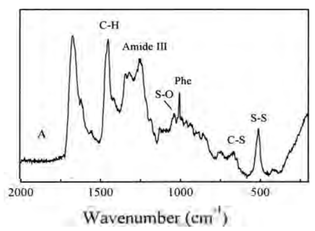

Figure 5: A raman spectra of keratin in white human hair [3], with chemical functional groups labeled.

Nanoindentation

- Nanoindentation provides local measure of modulus, or stiffness, by pressing a small tip into a sample (Figure 6a)
- A TI-950 Triboindenter (Hysitron, Inc) equipped with a Berkovich (3- sided pyramidal) tip was used
- Indents were performed to a depth of 1 micron and spaced by at least 15 microns
- The unloading curve is analyzed to calculate a modulus (E_r), or stiffness, for each location indented (Figure 6b)
- Average moduli for each whisker type (cat, rat) and orientation (transverse, longitudinal) were calculated using Excel

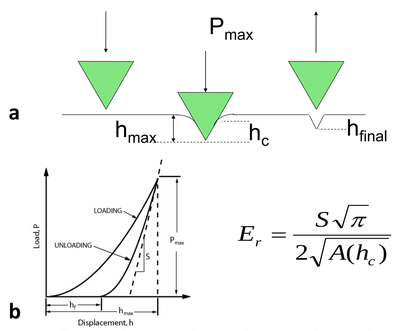

Figure 6: (a) Schematic of indentation with the Berkovich tip. **(b)** Sample indent load-displacement curve and equation used to calculate the modulus.

RESULTS

- Spectral peaks found in rat and cat whisker cortex (Figure 7) are similar to peaks found in pure keratin, including peaks around 500 cm^{-1} (disulfide Cys (S-S) stretch), 1000 cm^{-1} (symmetric ring breathing of Phe), and 2800-2930 cm^{-1} (C-H stretching)
- Analysis of the disulfide (S-S) peaks in cat and rat whiskers shows that the peak height and area are larger in cat than in rat spectra (Figure 8).
  - The disulfide was analyzed due to its association with material stiffness [7]
- Spectra collected in longitudinal and transverse whisker sections were similar

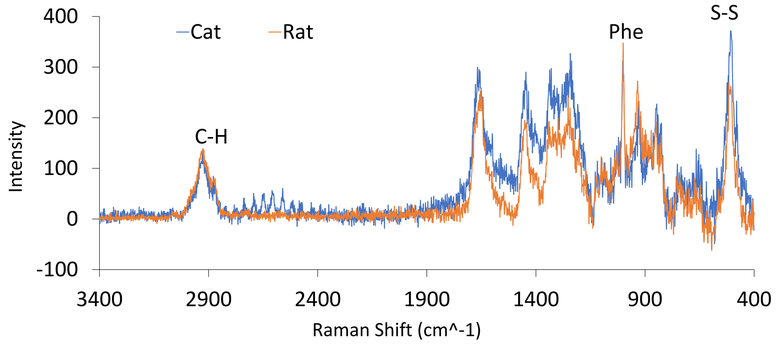

Figure 7: Comparison of cat and rat whisker cortex μRaman spectra. The spectra were processed with baseline correction using LabSpec6 software from HORIBA. Spectra were normalized to the C-H peak at 2900 cm^{-1}, a peak found in all proteins, using Excel.

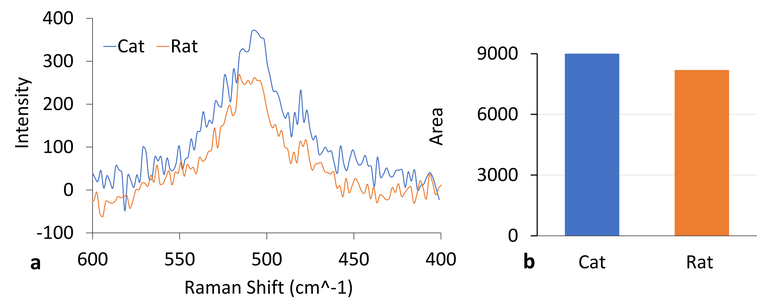

Figure 8: Comparison of disulfide (S-S) bond peaks of rat and cat whisker showing that both the peak height **(a)** and area **(b)** are higher in the cat spectra than in the rat spectra. Peak areas were calculated using Labspec6 software (cat area = 9074, rat area = 8204).

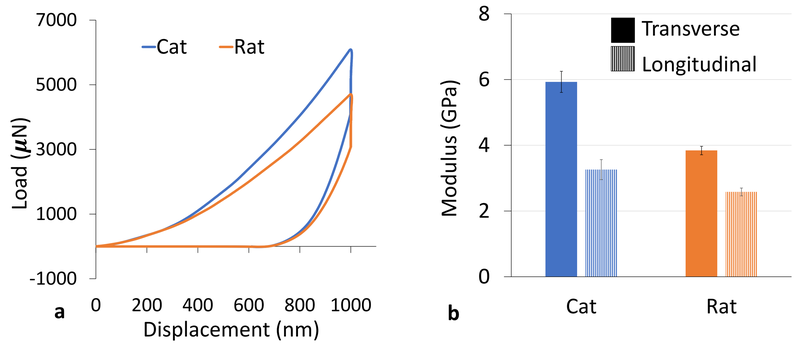

Figure 9: (a) Representative load-displacement curves for indents in transverse sections of cat and rat whiskers. **(b)** Comparison of mean E_r of cat and rat whiskers in transverse and longitudinal sections showing that cat whiskers are stiffer than rat whiskers and both species have higher moduli in transverse than in longitudinal sections. Error bars represent one standard deviation.

- It requires more force to indent to 1000 μm in cat than in rat whiskers, showing that cat whiskers are stiffer than rat whiskers (Figure 9a)
- Cat whiskers have a higher modulus than rat whiskers, and both cat and rat whiskers are stiffer in the transverse direction (Figure 9b)
  - **Transverse results**: 5.93±0.32 GPa in cat and 5.00±0.30 GPa in rat
  - **Longitudinal results**: 3.26±0.30 GPa in cat and 2.58±0.12 GPa in rat

DISCUSSION AND CONCLUSIONS

- Disulfide bond cross links (fig. 10), which are associated with forming stiffer materials [4], are more prominent in cat than in rat whiskers which imply that cat whisker keratin should be stiffer than rat whisker keratin
  - The results from nanoindentation support this conclusion from chemical analysis

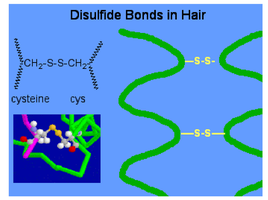

Figure 10: Cysteine S-S bond in hair structure that is responsible for the cross linking and folding of keratin. [5]

- For both species, the whiskers are stiffer in transverse sections than they are in longitudinal sections, suggesting that the whiskers are anisotropic
  - This is consistent with the whisker microstructure, which shows keratin fibrils aligned along the long axis of the whisker (Figure 2, C2 and R2)
- This study revealed that the increased flexibility of rat whiskers is due not only to having thinner, more tapered whiskers (shown in figure 11 than cats but also due to differences in the composition, and hence mechanical properties, of the keratin that makes up the whisker
- Future work will expand this study to include whiskers from other species, including horses that have passive whiskers, and computational modeling of whiskers to investigate the impact of differences in whisker structure and keratin mechanics on the whiskers' mechanical function as sensors

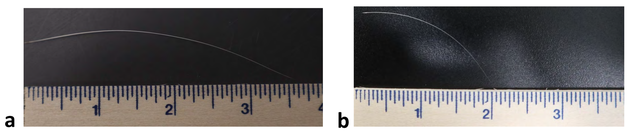

Figure 11: Photograph of **(a)** a cat whisker and **(b)** a rat whisker showing that the cat whisker is longer, thicker and less tapered than the rat whisker. This macrostructural property contributes to the increased flexibility observed in rat whiskers.

Research Impacts

- Researchers at MIT use harbor seal whiskers as an inspiration to design artificial whiskers that could effectively work as low-power sensors for underwater vehicles [5].
- Research in microstructures of rat and cat whiskers can be used to develop more robust on-land robotic monitoring systems adapted to different environments where human cannot go like the Mars Curiosity rover shown in Figure 12

Figure 12: The NASA robot's mission was to capture images and to find evidence of a habitable atmosphere on Mars. [2]

REFERENCES

[1] Diamond, M.E., et al. Nature Reviews Neuroscience (2008) 9: 601.
[2] Greicius, Tony. NASA (2019).
[3] Kuzuhara, A. J. APPL. POLYM. SCI. (2011) 122: 2680.
[4] Bornschlögl, T., et al. Proceedings of the National Academy of Sciences (2016) 113: 5940.
[5] Elmhurst College. VIRTUAL CHEMBOOK (2003).
[6] Chu, Jennifer. MIT News Office (2015).

Presented at the 2021 Susquehanna Valley Undergraduate Research Symposium

BORIS Expression in Transfected HCT116 Cells

Nathan Slotnick Oriana Balascio, and Dr. Kate Beishline
Bloomsburg University of Pennsylvania

Abstract

Recent studies suggest CTCF plays an important role in regulating eukaryotic telomeres, genomic structures at the ends of chromosomes that serve a protective role for the genetic material. CTCF is a chromatin and transcriptional regulator found in all human cells, and while it is evolutionarily conserved and unique, it only has one paralog, BORIS, which is naturally expressed in spermatocytes but has been shown to be turned on in many cancer cell models. Unlike CTCF, BORIS has no known role in telomere biology. The goal of this project is to create a cell model which can be utilized to study BORIS function in telomere biology. Here we produce and validate a BORIS fusion protein containing plasmid using a FLAG-HA-pcDNA3.1 plasmid backbone. We demonstrate the ability of the HCT116 cell line to express BORIS by RT-qPCR analysis of BORIS mRNA levels. Further studies will focus on validating BORIS protein expression by Western blot of immunofluorescence in these HCT116 cells prior to utilizing them to study telomere phenotypes. In addition, we are creating a model to express a tetracycline inducible form of the BORIS fusion protein to be used in side-by-side studies. Ultimately this research will allow the lab to address BORIS's role in telomere biology and shed light on how it may contribute to telomere stability in normal and cancer cells.

Background

Cell division is a crucial function to all life. For eukaryotic cells to divide, their genetic material needs to be replicated and packaged as chromosomes. This genetic material is stored in a cell's nucleus as Deoxyribonucleic acid (DNA). The genome will provide the template for a new daughter cell to create all the essential proteins and molecules through the process of the central dogma. At the ends of chromosomes is the telomere region. Telomeres are non-coding 5'-TTAGGG-3' repeats that protect the cellular genome during cell division and the life of the cell. During each cell division some of the telomere is lost but protects important coding DNA from being lost instead. Adjacent to the telomeres are the subtelomeric regions which play a key role in regulating the telomere stability and replication process. Subtelomeres contain conserved binding sites for the protein CTCF which plays a key role in mediating chromatin interactions. This CTCF binding is required for TERRA transcription, a long non-coding transcript produced from the subtelomere and telomere sequences, which plays a role in regulating telomere stability. Absence of CTCF proteins has been shown to inhibit TERRA transcription (Deng 2012, Beishline 2017). The only known paralog of CTCF is BORIS. While CTCF is expressed in all mammalian cells BORIS is only expressed naturally in spermatocytes and abnormally in some cancers. The role of BORIS is yet unknown in TERRA transcription and telomere maintenance, but preliminary data suggest in cancer cells it may antagonize CTCF function at telomeres. In previous studies the HCT116 cell line has been utilized to understand the role of CTCF in telomere regulation (Beishline 2017). This aim of this study is to create a model system from HCT116 cells, to express BORIS and study its role in regulating telomeres.

Methods

pCDNA-Flag-HA plasmid was obtained from addgene (#52535) and pINDUCER-BORIS plasmid was obtained by a collaborator and is previously published (Debruyne 2019). Plasmid DNA purification from bacteria was done using Invitrogen PureLink Quick Plasmid Miniprep and Maxiprep kit. PCR amplification of the BORIS insert was completed by using Thermo Scientific Phusion High- Fidelity PCR Master Mix kit with primers purchased and designed from IDT. PCR products and digested plasmid fragments were purified using Invitrogen PureLink Gel Extraction and PCR Purification Combo Kit. Plasmid and Insert ligations were completed using standard T4 ligase at a 1:4 ratio and then transformed into DC5α competent cells from Thermo Scientific. Invitrogen Lipofectamine 3000 reagent was used for plasmid transfection into HCT116 cells using manufacture instructions.

Results

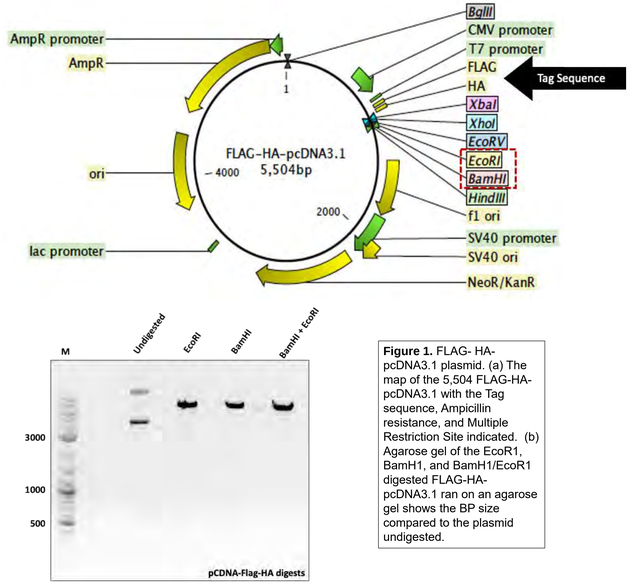

Figure 1. FLAG- HA-pcDNA3.1 plasmid. (a) The map of the 5,504 FLAG-HA-pcDNA3.1 with the Tag sequence, Ampicillin resistance, and Multiple Restriction Site indicated. (b) Agarose gel of the EcoR1, BamH1, and BamH1/EcoR1 digested FLAG-HA-pcDNA3.1 ran on an agarose gel shows the BP size compared to the plasmid undigested.

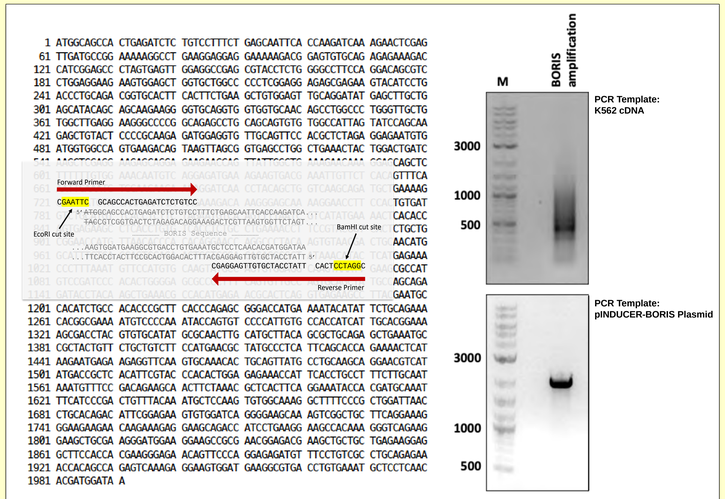

Figure 2. PCR amplification of K526 cDNA BORIS and pINDUCER- BORIS. (a)Forward and Reverse Primers for the BORIS Sequence. Primers were designed to bind to the 5' and 3' regions of the BORIS gene sequence attaching the necessary EcoR1 and BamH1 restriction enzyme sites. (b) Agarose gels of the K562 cDNA and pINDUCER-BORIS amplified BORIS insert. PCR from K562 cDNA sample yield a mixture of products with the primary being around 500bp. PCR from purified BORIS containing plasmid yielded a single band approximately 2000bp (the correct size for the BORIS gene insert).

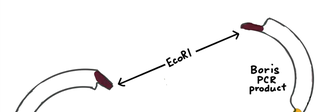

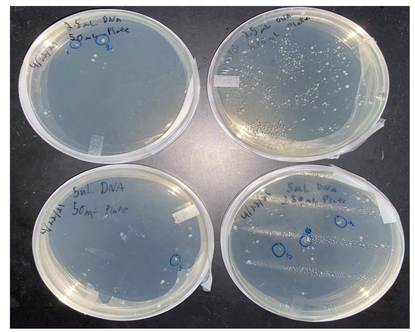

Figure 3: EcoR1 and BamH1 digested pcDNA plasmid and BORIS insert ligation. (a) Indication of restriction cut sites for ligation product. Ligation was completed at a 1:4 plasmid to insert ratio using T4 ligation. Ligation reaction was transformed in DH5α competent bacteria cells (b) Bacterial colonies selected for purification and sequence validation of BORIS insertion.

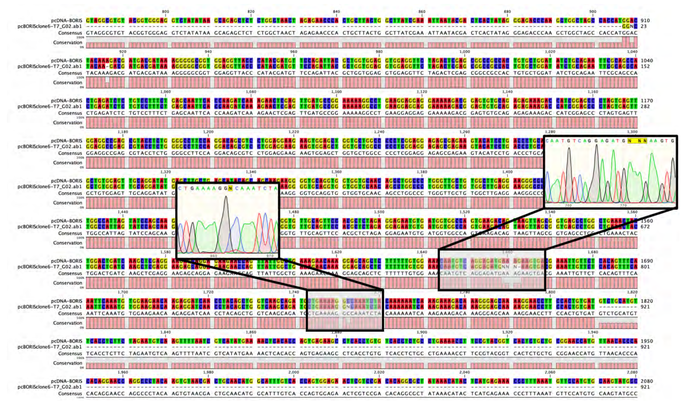

Figure 4: Initially purified plasmid DNA was validated by gel electrophoresis (data not shown) and potentially positive clones were sent for sequencing using primers that flank the 5' and 3' region (T7 and BGHR standard plasmid sequencing primers) of the newly inserted BORIS cDNA. Sequencing results for the 5' end (left panel) and 3' end (right panel) of the positive clone selected for further studies is shown. Two regions in the sequencing results for this clone were initially indicated as inconclusive (highlight in left panel) but were ultimately determined to be artifacts after further analysis of the sanger sequencing track data.

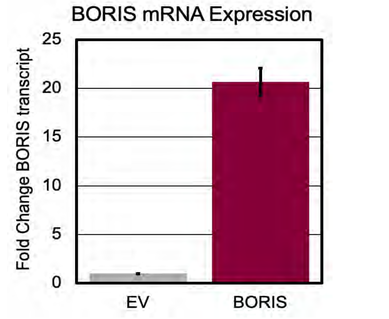

Figure 5: BORIS mRNA analysis. HCT116 colon cancer cells were transfected with pCDNA-Flag-HA-BORIS plasmid or empty vector plasmid and selected for greater then 14 days with geneticin antibiotic. RNA was collected from selected cells and purified from using Trizol. 2μg of RNA was utilized to generate cDNA using SuperScript IV VILO Master Mix with ezDNAse enzyme. 5 microliters of diluted cDNA was used to measure transcript levels using SYBRgreen PCR and primers for the BORIS mRNA as well as GAPDH mRNA as a control. X-axis labels indicate cell line; EV, empty vector; BORIS, BORIS expressing. Fold change in transcript level was calculated using the $\Delta\Delta$Ct method.

Future Directions

Further validation of the protein expression levels of BORIS in transfected cells will be completed using western blot and immunofluorescence with an an anti-BORIS and anti-FLAG antibodies. In addition, we are developing an HCT116 cell line expressing a Tetracycline inducible BORIS-HA fusion protein. This construct is virally introduced into HCT116 cells using a lentiviral infection system. These virally transduced cells have been produced and will validated for inducible expression of BORIS alongside the transfected cells in our further studies.

Acknowledgments

We thank Rani George MD, PhD (Dana-Farber Cancer Insitute, Boston, MA) for donation of the pINDUCER-BORIS plasmid, and the lab of Jane Azizkhan-Clifford (Drexel University College of Medicine; Philadelphia, PA) for providing us with the 293T cells and the retrovirus packaging vectors being used for the generation of the virally inducible BORIS construct. This work is generously support by the Bloomsburg University URSCA program and the Jessica S. and Stephen R. Kozloff Faculty Fellowship.

References

1. Beishline, K et al. (2017). CTCF driven TERRA transcription facilitates completion of telomere DNA replication. *Nature Communications, 8*(1).
2. Deng, Z. et al. . (2012). A role for CTCF and cohesin in subtelomere chromatin organization, TERRA transcription, and telomere end protection. *The EMBO Journal, 31*(21), 4165-4178.
3. Debruyne, D. et al. (2019). BORIS promotes chromatin regulatory interactions in treatment-resistant cancer cells. Nature. Aug; 572(7771): 676–680.

Commissioning Process for the High Rigidity Spectrometer (HRS)

George Sun, Matt Amthor

Department of Physics & Astronomy, Bucknell University, Lewisburg, PA

Introduction

The HRS will play a key role in the soon-to-be-completed Facility for Rare Isotope Beams (FRIB), which will produce rare isotopes for study. The HRS will focus the product ions of a nuclear reaction and separate them by momentum, scattering angles, etc.

Our goal is to design and simulate the calibration process of the HRS and thus reliably correct the beam focusing errors after the HRS is built.

Methodology

- Ion-optical systems focus, bends and, separates the charged particle beam by applying magnetic fields.
- HRS consists of six (6) focusing quadrupoles and two(2) bending dipoles.

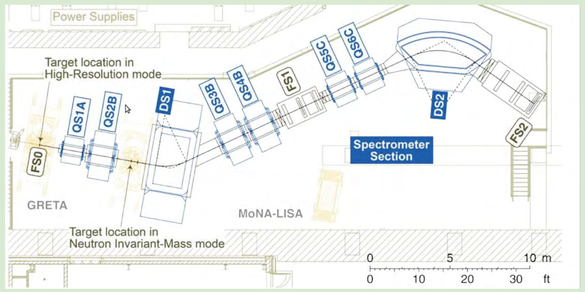

Figure1: The Engineering Diagram of the HRS. Multiple Focusing terms labeled as QS.

- Mapping matrix describes how the beam transfers through the system.

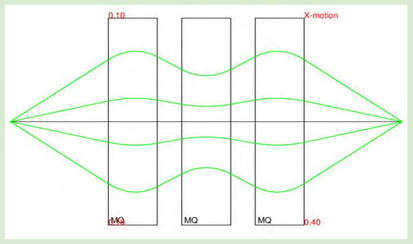

Figure 2. An example plot of a beam traveling through a quadruple triplet. The output position is not dependent on the input angle, implies mapping matrix term (x|a)=0. This is equivalent to a horizontal point-to-point focus.

- qMatrix describes how sensitive the mapping matrix terms are to the quadrupoles.[1]

Change in mapping terms ***qMatrix*** ***Field strength adjustments***

$$\underbrace{\begin{bmatrix}\delta(x|a)\\ \delta(y|y)\\ \delta(a|dk)\\ \delta(a|x)\end{bmatrix}}_{\vec{\delta}} = \underbrace{\begin{bmatrix}Q_{11} & Q_{12} & Q_{13} & Q_{14}\\ Q_{21} & Q_{22} & Q_{23} & Q_{24}\\ Q_{31} & Q_{32} & Q_{33} & Q_{34}\\ Q_{41} & Q_{42} & Q_{43} & Q_{44}\end{bmatrix}}_{\mathbf{Q}} \times \underbrace{\begin{bmatrix}\delta M_1\\ \delta M_2\\ \delta M_3\\ \delta M_4\end{bmatrix}}_{\vec{M}}$$

Equation 1: Matrix equation of qMatrix relationship

$$\vec{\delta} = \mathbf{Q} \times \vec{M}$$

$$\mathbf{Q}^{-1} \times \vec{\delta} = \mathbf{Q}^{-1} \times \mathbf{Q} \times \vec{M}$$

$$\vec{M} = \mathbf{Q}^{-1} \times \vec{\delta}$$

- Correct the quadrupole tunes by solving the matrix equation

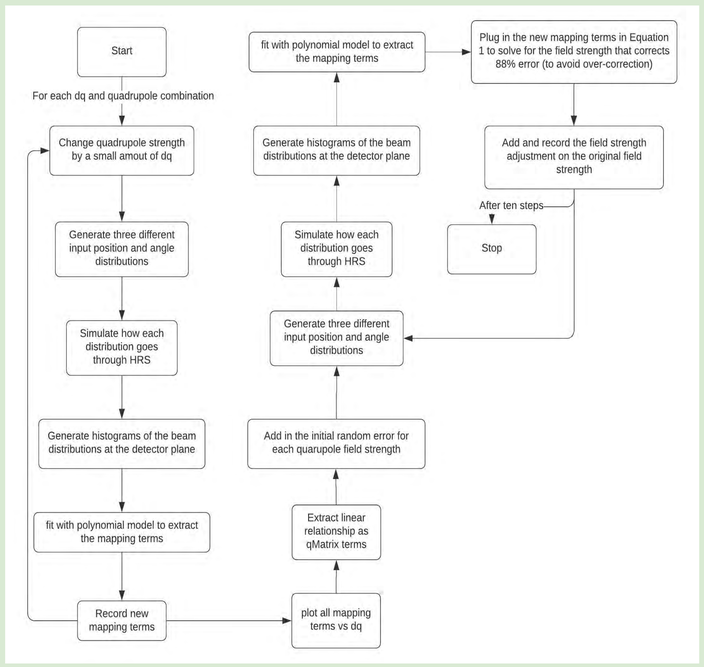

Figure 3: Flow chart of the calibration algorithm

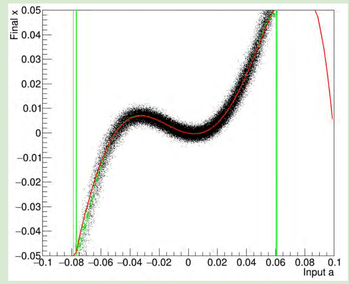

Figure 4: An example of the histograms and polynomial fit (red line) of the mapping term (x|a)

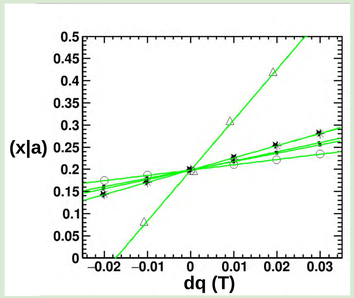

Figure 5: Mapping term (x|a) vs. the field strength change for each quadrupole.

Result and Discussion

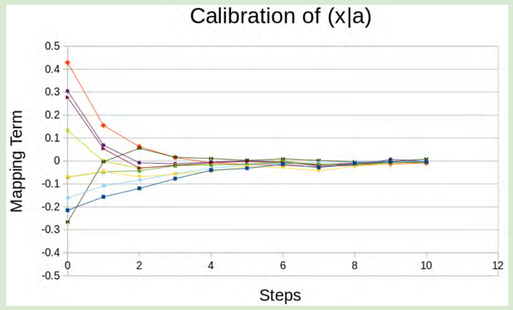

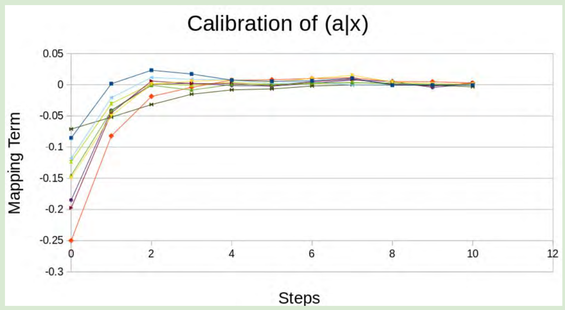

Figure 6 : Evolution of four mapping terms as the calibration iterations proceed.

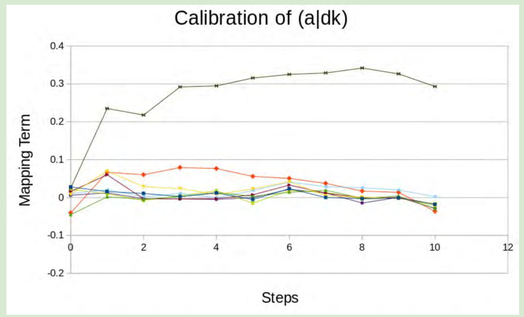

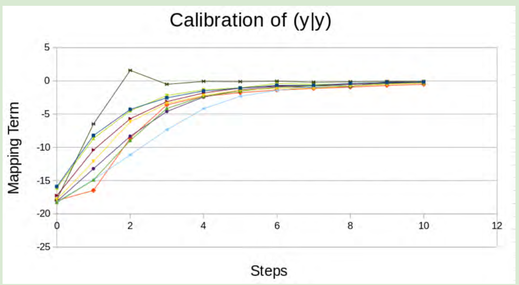

Figure 6 continued

- Repeatably successful in correcting random initial error smaller than 0.03T
- Three input beam distributions are applied for more reliable mapping term extractions.

Future Work

- Apply the commissioning process to the HRS after it is built and optimize the algorithm based on the realistic results.
- Apply also to the High Transmission Beam Line, the upstream section of HRS

Acknowledgements and References

Special thanks to Michigan State University and Physics & Astronomy Department of Bucknell University.

[1] Study of the Isovector Non-spin-flip monopole resonance via the super-allowed Fermi type charge exchange reaction, Y. Sasamoto (2012)

[2] FRIB High Rigidity Spectrometer Conceptual Design Report, R. G. T. Zegers et al. (2019)

Particle Swarm Optimization for High Rigidity Spectrometer

Yicheng Wang, George Sun, Matt Amthor.

Department of Physics and Astronomy, Bucknell University, Lewisburg, PA.

Goals

- Find reliable sets of parameters to optimize the High Rigidity Spectrometer (HRS) system at the Facility for Rare Isotope Beam (FRIB).
- Maximize the transmission rate of fission fragments in the HRS system.

Background

- **Ion optics**
  - Passing a charged particle beam through multipoles and dipoles is like passing a light beam through lenses
  - Multipole: to focus or defocus the beam.
  - Dipole: to bend the beam / separate by momenta.

- **High Rigidity Spectrometer (HRS)**
  - Used to separate and characterize particles by different momenta, reaction angles, etc.
  - Consists of six multipoles and two dipoles.

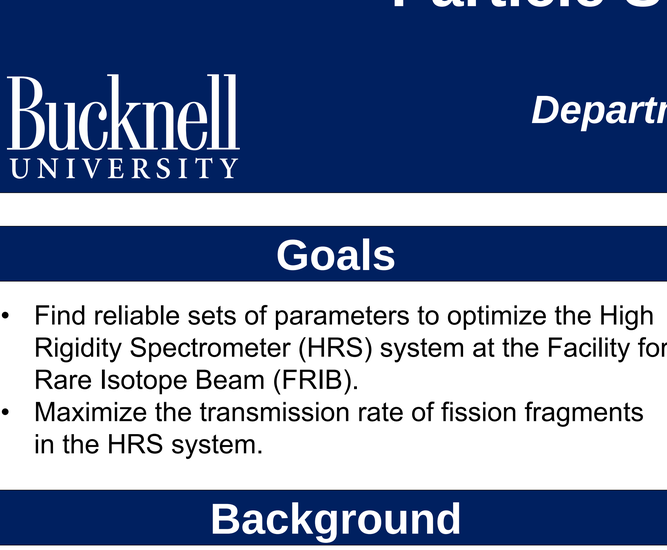

Figure 1: (a) Ray envelope of HRS in first order; (b) Ray envelope of HRS in fifth order.
*MSS = dipole, M5 = multipole.

- **Computer simulation: COSY INFINITY**
  - Describes the changes in the positions and angles of particles as they go through bending and focusing magnetic field elements.
  - Use Taylor expansion techniques.
  - Able to simulate higher order optical aberrations.

Method

- Particle Swarm Optimization (PSO)
  - Basic principle
    - Particles explore the solution space over a series of steps
    - Particles explore like birds in 3D looking for food.
  - Key factors
    - Inertia - how much velocity from the last step do swarm particles keep
    - Acceleration - how fast do you accelerate toward more attractive region

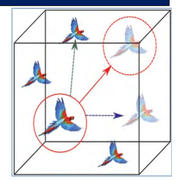

(Objective value) = (1.0 – transmission rate) … (*lower* is better)

- Testing stage one
  - Explored a wide parameter space in (inertia, acceleration) [1] to optimize HRS beam transmission.
  - Found the best performance with the parameter setting (0.85, 0.4).

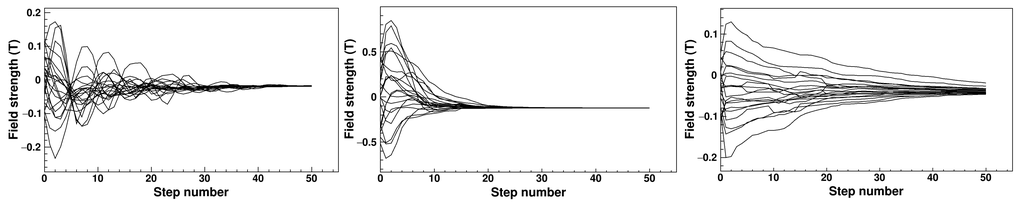

Figure 2: (a) Underdamped swarm plot (0.85, 0.4); (b) Critical damped swarm plot (0.475, 0.25); (c) Overdamped swarm plot (0.1, 0.1).

- Testing stage two
  - Explored the parameter space around (0.85, 0.4).
  - Each setting was tested 20 times with different initial randomization.

Result

Analyze the best 60% and 80% of the data for each set because we want to obtain good results at least 60% of the time for a good parameter setting.

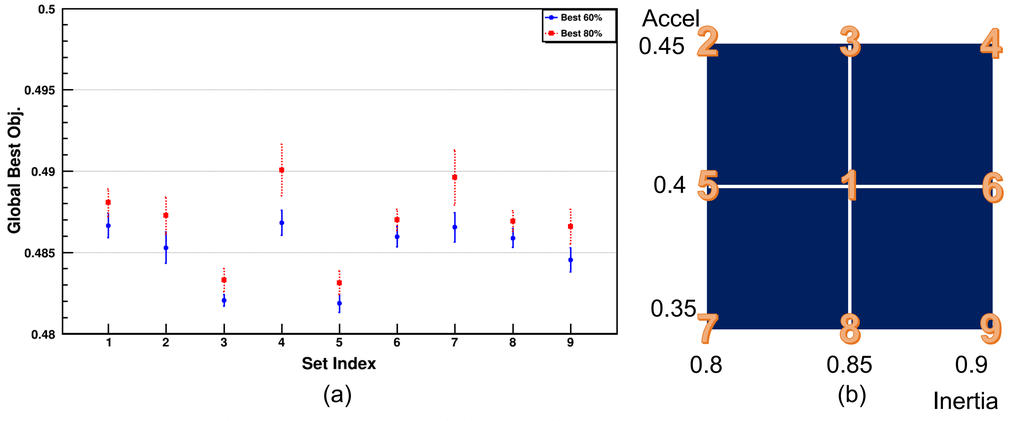

Figure 3: (a) Plot of the mean of the best 60% and 80% of the final obj. values with the error being the standard deviation of the mean; (b) Set index location in parameter space.

Results for two different tunes

- Two different energy ranges of the particle beam.
- Transmission rate without optimization: 40% for centered energy tune and 57.5% for highest transmission energy tune.

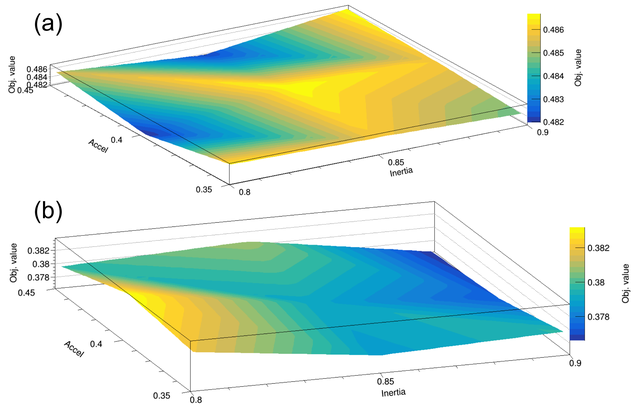

Figure 4: (a) Parameter space for centered energy system; (b) Parameter space for highest transmission energy system.
*Both graphs have the mean obj. value for best 60% in z axis and parameters from Figure 3(b).

Conclusion

- PSO depends on different types of tunes for the same system.
- The best parameters for the PSO for these two tunes are: (0.85, 0.45) and (0.8, 0.4) for centered energy (improved by 30%), (0.9, 0.45) for highest transmission energy (improved by 10%).

Future work

- Test on different tunes for the HRS system
- Test on different ion optical systems, e.g. High Transmission Beam Line (HTBL) system.

References

[1] Trelea, C. The particle swarm optimization algorithm: convergence analysis and parameter selection. *Information Processing Letters* (2003).
[2] Zegers, R. G. T., et al. FRIB HRS Conceptual Design Report (2019)
[3] Amthor, A.M., Schillaci, Z.M., et al. Experimental test of an online ion-optics optimizer. *Nucl. Inst. and Meth. A*. (2018)

Acknowledgements

This research was made possible through funding from Michigan State University.
Thanks to the Engineering Computing Support Team at Bucknell University for technical support.

The limits of chronic infection induced protection during secondary infection in *Drosophila melanogaster*

Abigail Wukitch, Alexa Patel, and Moria Chambers
Bucknell University

Background

- Live chronic infections induced via bacterial injection can provide protection against future lethal bacterial infections in *D. melanogaster*
- Bacterial injections into the thorax are more deadly than equivalent abdominal injections[1]
- Chronically infected flies exhibit unregulation of antimicrobial peptide gene expression
- Tolerance is the ability of a host to limit the damage caused by a pathogen as opposed to resistance which directly kills or limits pathogen growth[2, 3]

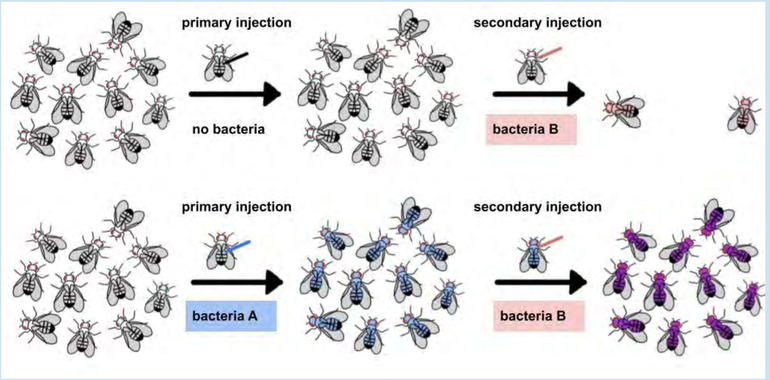

Questions

- What aspects of the immune system are changed by the presence of a live chronic infection that improves the ability for the fly to survive?
- How can the protection induced by chronic infection be modulated?
  - What is the result of different secondary doses?
  - What is the result of different primary doses?

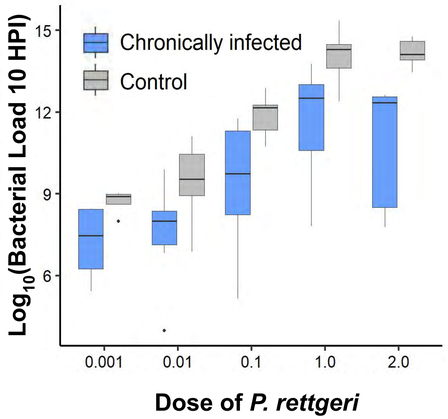

Results

Chronic infections improved both resistance and tolerance.

Flies carrying a chronic infection of *Serratia marcescens* had lower bacterial loads (improved resistance) 10 hours post infection (HPI) and improved survival at similar bacterial loads (improved tolerance) following a secondary infection with *Providencia rettgeri*.

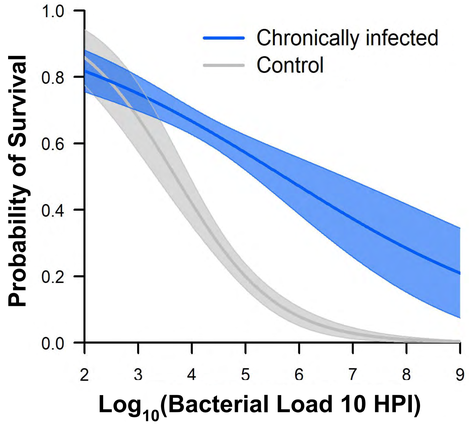

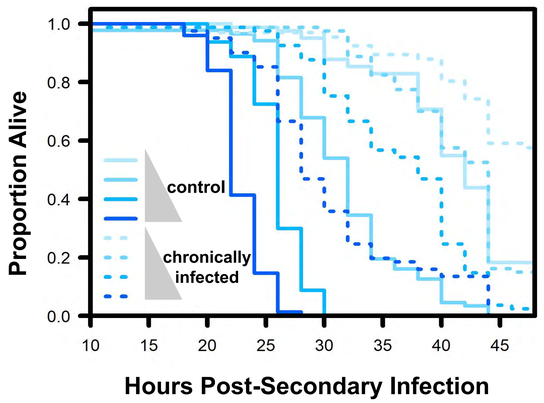

The protection from chronic infections can be very strong.

Flies were first infected with *S. marcescens* to establish chronic infection and then infected with *Providencia sneebia* at a range of doses. Even at low doses of *P. sneebia* most control flies died, while chronically infected flies were better able to survive the infection.

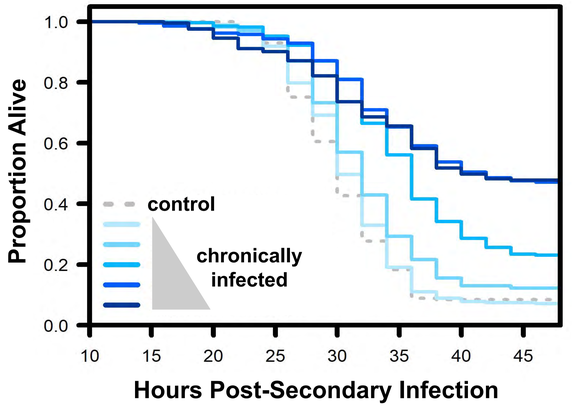

There is a minimum dose required to establish a protective chronic infection.

Flies were infected with *S. marcescens* at a range of doses to induce chronic infection and then infected with *P. sneebia*. The minimum dose of *S. marcescens* results in worse survival for the doubly infected. At the highest primary dose tested the protective effect remains but is weaker.

Future Directions

Exploring antimicrobial peptides (AMPs)

An upregulation of AMPs may provide a mechanistic explanation for the improved resistance in chronically infected flies. To test this hypothesis we will:

1) Compare different AMP levels of control and chronically infected flies 7 days post infection
2) Determine if there is correlation between greater AMP upregulation and higher chronic infection doses
3) Identify differences in AMP expression between chronically infected flies after secondary infection and control flies
4) Explore if chronically infected flies lacking AMP genes are protected

Exploring chronic infection in females

Females may have difference in the protective phenotype due to sexual dimorphic energetic burdens of reproduction in *Drosophila*. To test this hypothesis we will:

1) Determine if the protective effect exists
2) Analyze differences in resistance and tolerance in chronically infected females

Acknowledgements: The Chambers' lab at Bucknell University for teaching techniques and assistance with fly main. The Presidential Fellow's Program, the Russo Fund for Undergraduate Research in Biology and Chemical Sciences, and the Bucknell Biology Department for funding.

References

1) Chambers, M. C., Jacobson, E., Khalil, S. & Lazzaro, B. P. Thorax Injury Lowers Resistance to Infection in Drosophila melanogaster. *Infect. Immun.* **82**, 4380–4389 (2014).\
2) Pandey, U. B. & Nichols, C. D. Human Disease Models in Drosophila melanogaster and the Role of the Fly in Therapeutic Drug Discovery. *Pharmacol. Rev.* **63**, 411–436 (2011).
3) Prendergast, C. & Chambers, M. C. *Dissecting the Dynamics of Co-Infection in Drosophila Melanogaster*. 5 (2016).

What happens when you cross plant species with two distinct sexual systems? An ex situ hybridization approach

Morphometric analyses confirm that the pollen recipient influences the F1 morphology to the greatest extent; further analyses are being conducted on the F2 and subsequent generations.

Diamanda A. Zizis[1], Tanisha M. Williams[1], Christopher T. Martine[1]
1 Bucknell University Department of Biology

Project Goal

To assess how the andromonoecious and dioecious sexual systems manifest in Australian *Solanum* hybrids, relative to the parent's role as the pollen donor and pollen recipient.

Background

The evolution of the dioecious sexual system, in which pistillate and staminate flowers grow on separate plants, has been an area of intrigue in biology since Darwin's time (Anderson & Symon 1989). *Solanum* species display not only the rare dioecious system, occurring in only 6-10% of angiosperm species, but also the andromonoecious and hermaphroditic sexual systems, rendering them an ideal group to study sexual system evolution (Renner and Ricklefs 1995; Renner 2014). While current research suggests the origin of dioecy from andromonoecy in Australian *Solanum* (Martine & Anderson 2007), the observation of a dioecious hybrid evolving from an originally andromonoecious species would provide compelling evidence for the origin of andromonoecy first as an intermediate from hermaphroditism, and then a final transition to dioecy as a means to increase genetic variation by decreasing self incompatibility (Anderson & Symon 1989). Additionally, this would inform phylogenies where the origin of dioecy is not yet understood.

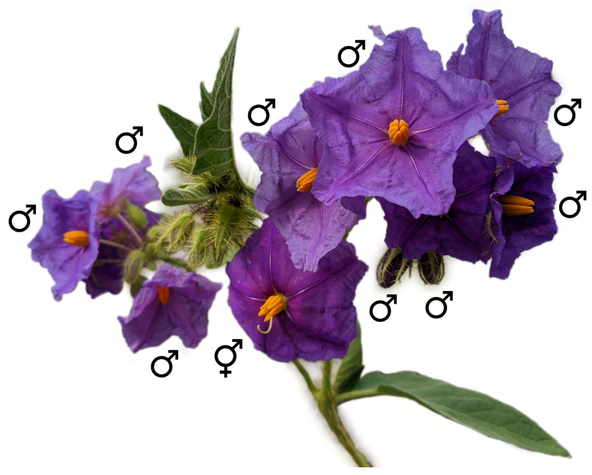

Figure 1 Andromonoecious sexual system displayed on the hybrid species flowers.

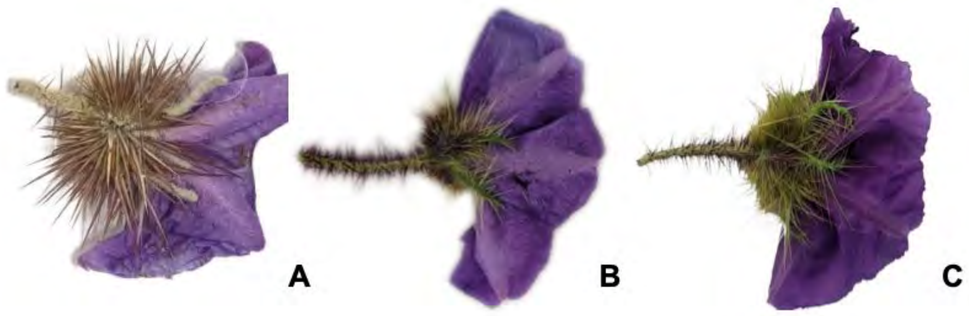

Figure 2 Hermaphroditic flower morphology: (A) *S. dioicum* (pollen donor species; functionally pistillate), (B) *S. ultraspinosum* (pollen recipient species), (C) hybrid.

Figure 3 Staminate flower morphology: (A) *S. dioicum* (pollen donor species), (B) *S. ultraspinosum* (pollen recipient species), (C) hybrid.

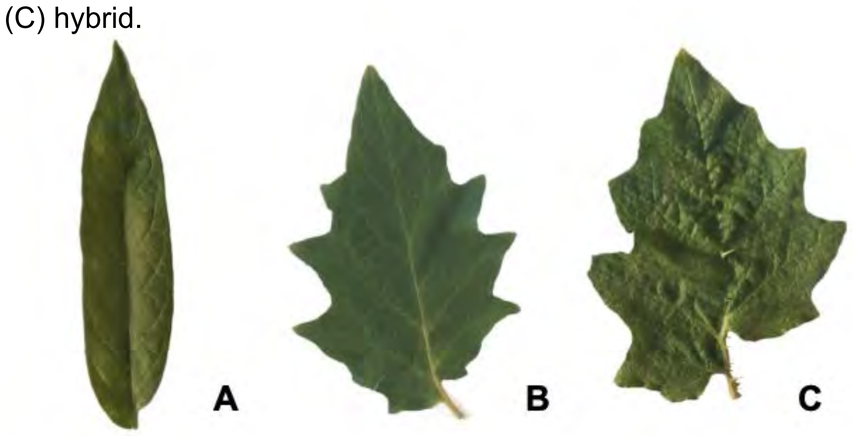

Figure 4 Leaf morphology: (A) *S. dioicum* (pollen donor species), (B) *S. ultraspinosum* (pollen recipient species), (C) hybrid.

Methods

Solanum hybrid seeds were acquired from a series of crosses and self-compatibility tests conducted by Dan Hayes in 2018 using 16 *Solanum* species (Hayes 2018). *Solanum dioicum* W. Fitzg. (dioecious) and *Solanum ultraspinosum* A.R. Bean (andromonoecious) were chosen as our study species, because their differing sexual systems enable us to observe how the andromonoecious and dioecious sexual systems manifest in hybrids. Morphometric analyses were conducted both in the greenhouse and using ImageJ measurement software, with an emphasis on reproductive traits. F1 individuals were hand pollinated by Drs. Chris Martine and Tanisha Williams during the summer of 2020. F2 hybrid plants are currently growing. Once these plants have grown to maturity, we will be conducting the same measurements and analyses with the F2 generation.

Key Findings and Future Analyses

Hybrid Morphology:

- The morphology of F1 hybrids is most heavily influenced by the pollen recipient, and as such, all hybrids displayed the andromonoecious sexual system
- Based on the Principal Component Analysis (PCA) it appears the hybrids are morphometrically independent of both parents

Future Analyses:

- The same measurements will be continued in order to detect changes in the F2 and subsequent generations
- The absence or presence of inaperturate pollen is a key characteristic, in addition to a change in floral architecture, which would indicate changes incurred due to the pollen donor's influence

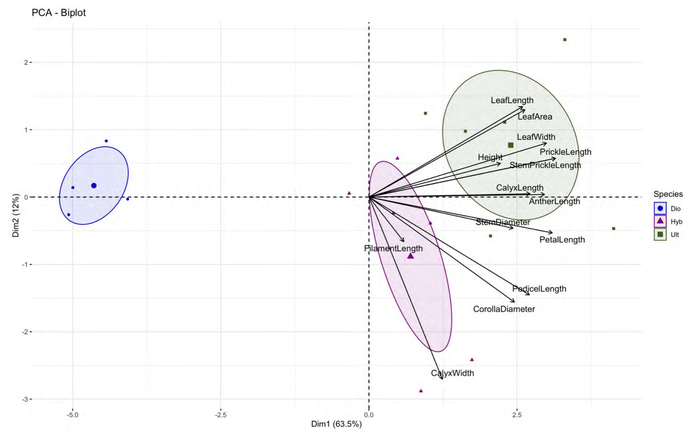

Figure 5 Species PCA: the hybrids are close, but independent of the pollen acceptor species, indicating hybridization between *Solanum diocium* and *Solanum ultraspinosum*

Implications

The ability to track changes in the sexual characters, if present, will allow for a clearer understanding of how hybridization occurs in *Solanum* species, and especially as to how the rare dioecious sexual system evolved. Particularly, if the loss of staminate function is observed, it will be indicative of a key transitional step from andromonoecy to dioecy in the hybrid sexual system, and support the established hypothesis of diocey from andromonoecy.

Anderson, G. J., & Symon, D. E. 1989. Functional dioecy and andromonoecy in *Solanum*. *Evolution 43*(1): 204-219.

Renner, S. S. 2014. The relative and absolute frequencies of angiosperm sexual systems: Dioecy, monoecy, gynodioecy, and an updated online database. *American Journal of Botany* 101: 1588–1596.

Martine, C.T., & Anderson, G.J. 2007, July. Dioecy, pollination and seed dispersal in Australian spiny *Solanum*. In *VI International Solanaceae Conference: Genomics Meets Biodiversity* 745 (pp. 269-285).

Hayes, Daniel S. 2018. Ex situ interspecies crossing rates infer importance of geographic barriers in speciation among closely related Solanum species of the Australian Monsoon Tropics. *Honors Theses*. 447.

Renner, S.S. and R. E. Ricklefs. 1995. Dioecy and its correlates in the flowering plants. *American Journal of Botany.* 82: 596-606.

Support: David Burpee Endowment and the Presidential Fellowship

Bucknell UNIVERSITY BIOLOGY DEPARTMENT